NASA-TM-72870 19800002036

NASA Technical Memorandum 72870

SHUTTLE ORBITER RADAR CROSS-SECTIONAL ANALYSIS

Dale W. Cooper and Robert James

October 1979

NASA

NASA Technical Memorandum 72870

SHUTTLE ORBITER RADAR CROSS-SECTIONAL ANALYSIS

Dale W. Cooper
Dryden Flight Research Center
Edwards, California

and

Robert James
James and Associates
Lancaster, California

National Aeronautics and
Space Administration

1979

SHUTTLE ORBITER RADAR CROSS-SECTIONAL ANALYSIS

Dale W. Cooper
Dryden Flight Research Center

and

Robert James
James and Associates

INTRODUCTION

Due to the absence of a radar beacon on the shuttle orbiter during the planned orbital flight tests (OFT) commencing tentatively in March 1980, skin tracking must be used by all assisting radars prior to the landing at Rogers Dry Lake at Edwards, California. Radar cross-section information is necessary to predict the range at which initial radar lock-on can be achieved and to establish search procedures to be used prior to acquisition.

During these orbital flight tests, the Air Force Space and Missile Test Center (SAMTEC) radars at Vandenberg, California will initially acquire the orbiter and send parallax-corrected acquisition data to both the Dryden Flight Research Center (DFRC) and the Air Force Flight Test Center (AFFTC) radars at Edwards, California where the final landing will be made (ref. 1). Because of the supersonic shuttle velocities, tracking time from first acquisition to landing will be only 7 minutes. With no engines on the orbiter to provide major course corrections, early acquisition is necessary to insure the safety of the landing.

Theoretical and model simulation studies on signal-to-noise levels and shuttle radar cross section were performed for NASA. However, to derive a more accurate radar cross-sectional profile for the space shuttle orbiter, range and angle data and receiver automatic gain control (AGC) voltages were recorded at both the AN/FPS-16 and AN/MPS-19C radars during the free-flight phase of the third approach and landing test (ALT) flight on September 23, 1977. After the mission, each radar was calibrated by tracking a 0.25 m^2 balloon-carried target using the same power and system configuration as had been used for the orbiter tracking mission.

Subsequently, the radar data were combined with orbiter heading and altitude data obtained from the time-tagged Johnson Space Center (JSC) flight measurements listings. A computer program then used these data to calculate the impinging angles for each of the two C-band signals with respect to the orbiter body axes and matched these results with the computed cross-sectional values derived from the two sets of radar measurements.

Extremely good correlation was found in the cross-sectional values derived from the two sets of radar data, and cross-sectional plots were made for the aspect angles of interest in the OFT tracking task.

SYMBOLS

B	noise bandwidth of intermediate-frequency amplifier referenced to 1 hertz, dB
G	gain of antenna over isotropic gain, dB
L	transmitting and receiving line losses, dB
$\overline{NF}_0$	operating noise figure, dB
P_t	transmitted power referenced to 1 watt, dBw
R	range referenced to 1 nautical mile, dB
S/N	ratio of receiver signal power to noise power, dB
λ	transmitted wave length referenced to 1 hertz, dB
σ	radar cross section referenced to 1 m^2, dBm^2

TRACKING RADARS

Pre-Mission System Calibrations

Prior to the mission, each of the two radars underwent the various alinement and calibration checks specified in the appropriate pre-mission operational validation document. The pre-mission validations performed included the normal oscillator alinements, deviation checks, offset checks, range calibrations, and frequency adjustments. In addition, each of the radars was given a careful AGC calibration, both with parametric amplifiers (paramps) on and with paramps off. The calibration data were recorded and served as a basis for the post-flight conversion of the AGC voltages to signal-to-noise values for each even second during the flight.

System Configuration

During the free-flight phase of the mission, the AN/FPS-16 radar was operated at 50 percent power, paramps off, and in the dual local oscillator mode. In the dual local oscillator mode, both the skin and beacon oscillators are active. Although the system continues to track the target by means of the beacon return, the skin return is also processed in the system such that the skin AGC values can be observed and recorded using the system's chart recorder. The use of the dual local oscillator mode reduces the angle noise that would otherwise cause the apparent source of the return to wander back and forth about the physical center of the target. Since the beacon was used on the ALT missions, the dual mode feature provided a convenient method for obtaining the simultaneous skin track data needed for the cross-section calculations. During the flight, the AN/FPS-16 range, azimuth, and elevation data were recorded in digital form by the Aerodynamic Test Range (ATR) real-time tracking data processing system. AGC values from the AN/FPS-16 were recorded, along with IRIG-B timing, using the site's strip chart recorder.

During the flight, the AN/MPS-19C radar was operated at 100 percent power, paramps off, and in the skin local oscillator mode. A skin track was maintained from the time of launch until runway touchdown, providing tracking data for the body-axis azimuth aspect angles from 253° through 360° to 135°. The elevation aspect varied from 45° during a 59° bank maneuver to negative values in excess of -30°. Range, azimuth, and elevation (r, a, el) data and AGC voltages were recorded continuously on the site's magnetic tape recorder.

Post-Mission System Calibration

Immediately following the flight, a 0.25 m^2 balloon-carried target was released and tracked by the two radars. AGC values from both radars were plotted using strip chart recorders. Each even 991.4 meter (1 kiloyard) point on the plot was identified as the range increased. All tracking system configurations were the same as used on the orbiter mission except that, in the case of the AN/FPS-16 radar, the calibration target was tracked in the single local oscillator mode. However, during a subsequent calibration run, the system was placed in and out of the dual mode several times, and it was found that the dual mode loss consistently measured 3.9 dB. This factor had to be applied to the AN/FPS-16 data obtained during the orbiter tracking mission since the system was operated in dual mode at that time.

For the AN/FPS-16 radar, the average cross-sectional value was -5.84 dBm^2, with a standard deviation of 1.09 dB for the 0.25 m^2 (-6.02 dBm^2) target. Correspondingly, for the AN/MPS-19C radar the average cross-sectional value was -6.26 dBm^2, with a standard deviation of 0.38 dBm^2. Thus, it can be expected that the shuttle orbiter cross sections provided by these radars are probably accurate within 1 dB or less.

DATA REDUCTION

To compute radar cross section as a function of the impinging angle of the radio-frequency (rf) energy on the body axis triad, it was first necessary to time correlate data from three separate sources. Body axis data were obtained from onboard inertial recordings. Radar signal-to-noise measurements were obtained from strip chart recordings of intermediate-frequency signal levels at each of the two tracking radar sites. Position data relative to each of the two radars were obtained from digital recordings of range, azimuth, and elevation from the two radars. Separate IRIG-B timing was provided for each of the recordings.

After the flight, each data set was combined and time correlated to provide the source material for a cross-sectional analysis based on the signal-to-noise measurements recorded at the two tracking radars. The source data set for each radar included:

1. IRIG-B time reference (even seconds).
2. Range, azimuth, and elevation (r, a, el) of the target at each even second.
3. Signal-to-noise ratio at each even second.
4. Body-axis angles measured on board the orbiter interpolated to each even second.

The impinging angle of the rf energy on the body of the orbiter was computed using the following sequence:

1. The orbiter's position was converted from spherical (r, a, el) coordinates into radar-centered, east-north-vertical- (ENV-) alined, right-hand Cartesian coordinates (app. A).
2. The Cartesian ENV coordinates were rotated to provide the orbiter's position referenced to a radar-centered Cartesian frame spatially offset from but in angular alinement with the earth-centered, right-handed Greenwich equatorial-polar (EFG) coordinate frame (app. B).
3. The orbiter position was then translated to the earth-centered EFG triad (app. C).
4. Having calculated the EFG coordinates of the orbiter, and knowing the EFG coordinates of the tracking radar, the ΔE, ΔF, and ΔG elements of the orbiter-to-radar vector were determined.
5. From the EFG coordinates of the orbiter, the geodetic position of the orbiter was determined (apps. D and E).
6. Knowing the geodetic coordinates of the orbiter and the elements of the orbiter-to-radar vector in the orbiter-centered, EFG-alined

coordinate frame, it was possible to rotate the position vector of the radar into an orbiter-centered, ENV reference frame (app. F).

7. Knowing the body-axis angles existing at the orbiter at the same instant in time, it was possible to rotate the orbiter-to-radar position vector through the body-axis Euler angles to obtain the position of the radar with respect to the orbiter-centered, right-handed, body-axis frame of reference (app. G).

8. The position of the radar with respect to the orbiter body axes was then converted from Cartesian to spherical coordinate form, thus providing the position of the radar in terms of azimuth (measured clockwise from the nose of the orbiter), elevation (measured positive upward from the wing-nose plane), and range.

This sequence of conversions, rotations, and translations provided the impinging angle of the rf energy referenced to the orbiter's body-axis triad for each second during the flight. It then remained to compute radar cross section from known radar parameters, the recorded signal-to-noise value, and the target range existing at each 1-second interval. This was accomplished using the classical radar equation (ref. 2) in logarithmic form:

$$\sigma = 4R + B + \overline{NF}_0 + L - P_t - 2\lambda - 2G + S/N$$

By correlating the radar cross-sectional computations for each even second in the analysis interval with the corresponding body axis angles of the impinging rf energy, a radar cross-sectional pattern was developed.

Because of the close range of the orbiter during the ALT phase of the program, no refraction correction was applied to the angular data. However, a refraction routine was provided in the program for future analyses, which will use data obtained during the orbiter's approach to landing from orbital missions.

LAMBERT TRANSFORMATION

In order to provide a qualitative measure of the tracking radar performance, the computer program used to reduce the radar data also included a Lambert transformation to permit the radar r, a, and el data to be converted into x-y position data that could be plotted using a standard mapping format. The results of these transformations, applied to both the AN/FPS-16 and AN/MPS-19C data, are shown in figures 1 and 2. Because the dual mode was used on the AN/FPS-16 radar, the position plot is somewhat smoother than the plot from the AN/MPS-19C radar, which was prepared from data obtained using the skin mode only. The orbiter tracks shown in figures 1 and 2 represent only the free-flight portion of the mission, and the end of the track represents the touchdown point. These Lambert plots also show the relative locations of the two radars. The proximity of the two radars to one another enabled some interesting comparisons to be made in the data, as will be shown later.

RESULTS AND DISCUSSION

The dotted curve in figure 3 shows the signal-to-noise measurements made at the AN/FPS-16 radar from the time of launch until 168 seconds after the launch. Because of the urgency of the tracking mission, it was necessary to discontinue the collection of signal-to-noise data at that time. The solid curve in figure 3 shows the signal-to-noise measurements taken at the AN/MPS-19C radar. In this case, since the radar was not prime, it was possible to devote the necessary effort to insure that valid signal-to-noise data were obtained from the time of launch until the time of touchdown. A skin track was maintained throughout this entire period, and all the AN/MPS-19C data are valid.

As was noted in figures 1 and 2, the two radars are situated in close proximity to one another and, at the tracking angles involved in this mission, did not have a great amount of parallax. When the two plots are compared, it is possible to see that the amplitude noise patterns on the two radars were quite similar. Both radars experienced a peak in the signal-to-noise data at about 66 seconds after launch. Numerous other similarities can also be seen in the data, not just in the general trend of the long-period changes, but also in the short-period noise patterns. The offset in some of the peaks is due to the fact that a certain amount of parallax did exist, and, except for points where the target was completely in line with both of the radars, a shadowing effect can be seen in the patterns. It is apparent from the figures that the noise amplitude of the two systems was very similar, both on a long-period and a short-period basis, indicating its source to be in the target's reflection and phase response to the incident wave front.

Figure 4 shows the computed radar cross section as a function of time after launch as calculated from the AN/FPS-16 and AN/MPS-19C data. Again, because of the parallax, the same aspect angle exposure was offset slightly in time between the two radars, but the similarities in both long- and short-period patterns are unmistakable. The peak at about 66 seconds after launch occurred as the orbiter's azimuth aspect angle quickly passed through 270° during the initial turn off the base leg. This broad peak that occurred from about 200 seconds to 270 seconds was caused by the slow broadside pass in the final stage of the landing approach.

Next, the cross-sectional data were correlated with aspect angle data and sorted to permit plots to be made of the cross-sectional values as a function of the body-axis azimuth aspect angles. To enhance the data point density of the plots, it was assumed that the cross-sectional profile for the left side of the vehicle was essentially the same as the cross-sectional profile for the right side of the vehicle. This permitted the data for the left and right sides to be combined into a plot covering the 180° aspect range from the nose to the tail. Provisions were also included in the program to allow any given elevation aspect window to be selected so that only those azimuth aspect points falling within the selected elevation window would be plotted. Again, the program was provided with the capability to plot the AN/FPS-16 and AN/MPS-19C data separately or as superimposed plots for comparison purposes.

Figure 5 provides data points on the elevation-slice-type cross section versus azimuth angle plots for the AN/FPS-16 radar. These plots extract radar cross section versus azimuth aspect angle data for elevation aspect angles of 0°, -10°, -20°, and -30°, respectively. In order to provide sufficient data in the plots to insure detection of any significant trends, it was necessary to use an elevation window of ±10°. An examination of these plots did not reveal any significant changes in the cross-sectional values over the ranges of elevation angles for which data were available.

Figure 6 provides the same type of data derived from the AN/MPS-19C radar for the same elevation slices. Again, it was not possible to detect any significant trends or changes in the cross section versus azimuth aspect angle plots for different elevation aspect angles.

The same data, but from both radars, are combined in the plots provided in figure 7. In these plots, the extremely good correlation that was obtained in the cross-sectional values computed from the two sets of radar data can be seen. Since none of the plots show significant trends in the cross-sectional values over the range of elevation angles available from the data, it would seem that a valid plot of cross section versus azimuth aspect angle would be obtained by accepting all of the elevation aspect angles in a single plot. This type of plot is provided in figure 8, which combines all the data from both radars.

From an analysis of figure 8, a radar cross section of 12 to 14 dBm^2 would be expected in the head-on aspect. This value may drop slightly, but not significantly, as the aspect angle shifts within about 25° of head-on. At about 25° azimuth aspect angle, the value of the cross section starts to climb to a broad maximum that extends from about 40° to 110°. It then trails off slowly in the aft quartering views. No data were obtained in the range from 140° to 180° aspect; however, these angles are not critical in the OFT tracking mission.

Figure 9 provides the same data as a smooth curve that eliminates the amplitude noise from scintillation and glint (refs. 3 and 4). Here again, the same pattern as previously described is presented.

Prior to ALT, a limited distribution publication entitled "A Comparative Analysis Between the AN/FPQ-6 and AN/FPS-16 Radars in the OFT Support Mission" (by Robert James, Rep. 013-76, James and Associates, Lancaster, Calif., Apr. 1976) was prepared under contract. In that document an estimate of the shuttle cross-sectional profile was made by various geometric comparisons and by consideration of cross-sectional profiles from comparably sized jet aircraft. As a result of these studies, it was concluded that the head-on aspect angle would provide a cross section of about 12 dBm^2. These estimates now seem to have been reasonably valid, although the broadside cross section was slightly underestimated. However, the estimates made at that time were intentionally conservative, for obvious reasons.

In that same document, an analysis indicated that, to achieve a 95 percent probability of lock-on with a 10^{-4} or less probability of false alarm, a 12 dB signal-to-noise return was required for both the AN/FPS-16 and AN/FPQ-6 radars. Using the tables provided in that publication, it can be determined that, for an approximate 12 dBm^2 radar cross-section target, a 12 dB signal-to-noise return would be expected in skin mode at about 600 nautical miles for the AN/FPQ-6 radars, and at about 225 nautical miles for the AN/FPS-16 radars. For the DFRC AN/FPS-16 radar, the first line of sight will probably occur around 380 nautical miles, so the range limitations of the 1 megawatt system will delay the acquisition for a short time until signal strength becomes sufficient for lock-on. Because of the increased power output, the AN/FPQ-6 class of radars should be capable of lock-on immediately after the first-line-of-sight conditions are attained.

CONCLUSIONS

From the data obtained during shuttle free flight number three, it appears that the orbiter vehicle exhibits cross-sectional characteristics approximating a comparably sized jet transport, except that the broadside peak may cover a broader range of aspect angles than would be the case with a conventional jet aircraft. Head-on cross-sectional characteristics are sufficiently good to provide immediate first-line-of-sight lock-on capability for the AN/FPQ-6 class of radars, but the AN/FPS-16 radars will experience some delay between first line of sight and the point where the signal-to-noise ratio of the return is sufficiently high to enable a lock-on to be achieved.

APPENDIX A.--CONVERSION OF TARGET RANGE, AZIMUTH, AND ELEVATION INTO RADAR-CENTERED EAST-NORTH-VERTICAL POSITION COORDINATES

Radar measurements of target position are made in spherical coordinates denoted by range (r), azimuth (a), and elevation (el). In this system, the radar is at the origin of the coordinate system and the fundamental plane passes through the radar and lies parallel to the reference spheroid horizon. The principal axis is taken as pointing northward along the meridian passing through the radar. This convention assumes that corrections are made in the measurements system to compensate for electrical and mechanical misalinements and for local geoid anomalies.

Conversion of target position from the radar-centered spherical coordinates to a radar-centered east (X), north (Y), and vertical (Z) Cartesian system is accomplished by the trigonometric relations given below.

$$X = r \sin a \cos el \tag{A1}$$

$$Y = r \cos a \cos el \tag{A2}$$

$$Z = r \sin el \tag{A3}$$

Figure A-1 is a superposition of the spherical and Cartesian systems. In the spherical system the convention is adopted such that elevation angles are measured positively from the fundamental plane, and azimuth angles are measured positively in a clockwise direction from north.

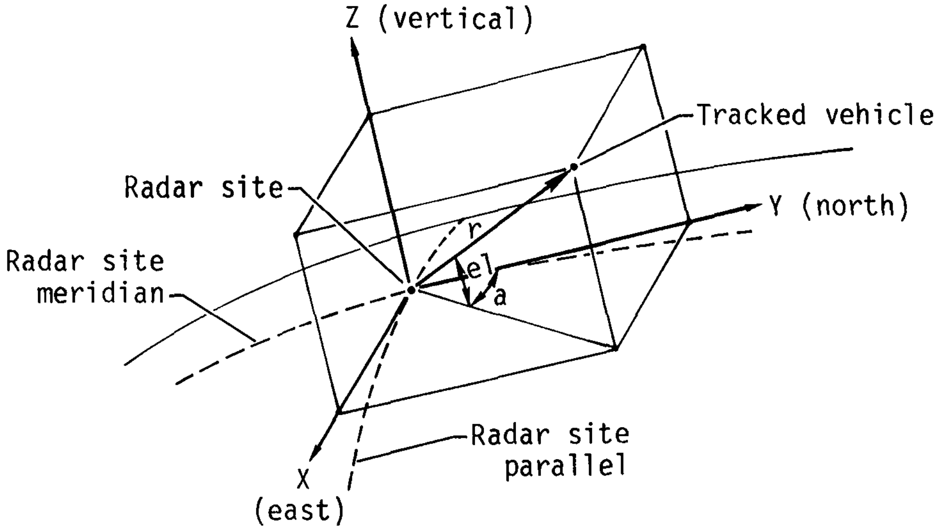

Figure A-1

APPENDIX B.--ROTATION OF TARGET POSITION COORDINATES FROM RADAR-CENTERED EAST, NORTH, AND VERTICAL ALINEMENT TO EQUATORIAL AND NORTH ALINEMENT

Target position given in terms of radar-centered east (X), north (Y), and vertical (Z) alinement is rotated into alinement with the spheroid-geocentric frame by use of the standard matrix relation:

$$\begin{bmatrix} E'' \\ F'' \\ G'' \end{bmatrix} = \begin{bmatrix} \sin W & \cos W \sin U & \cos W \cos U \\ \cos W & \sin W \sin U & -\sin W \cos U \\ 0 & \cos U & \sin U \end{bmatrix} \begin{bmatrix} X \\ Y \\ Z \end{bmatrix} \qquad (B1)$$

where E", F", and G" make up a right-handed Cartesian system whose principal plane is the equatorial plane of the reference spheroid and whose principal axis is parallel to the axis passing from the geocentric center through the north zenith of the reference spheroid. The symbols U and W represent the geodetic latitude and longitude of the radar site.

Figure B-1 pictorially shows the relation of the target's position coordinates in the two reference frames. The elements of the target-to-radar position vector are obviously the negative of the elements of the radar-to-target position vector.

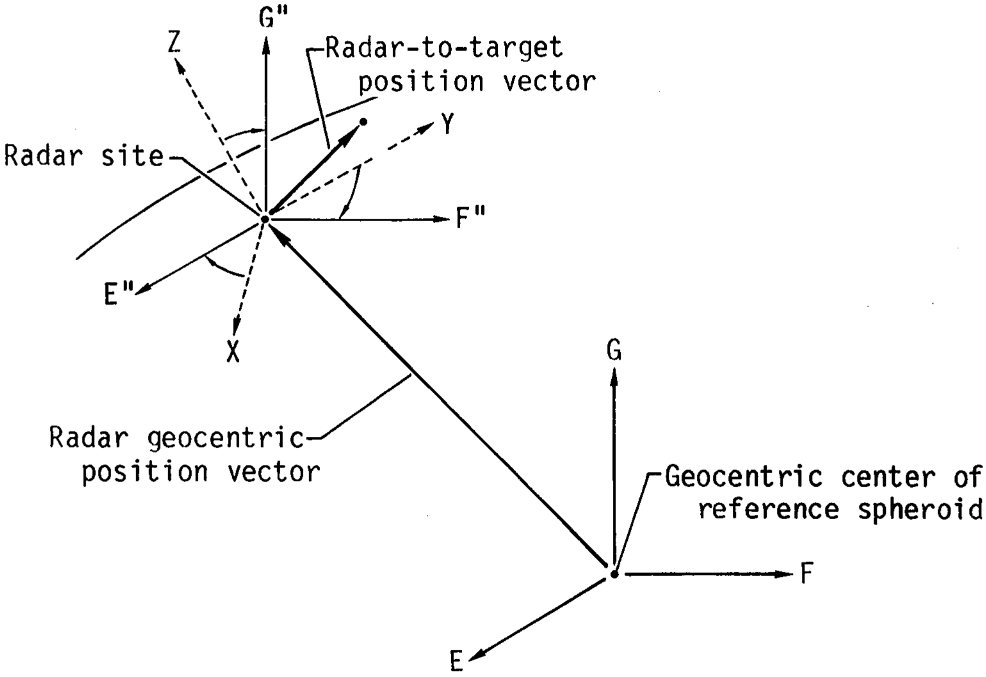

Figure B-1

APPENDIX C.--TRANSLATION OF TARGET POSITION COORDINATES FROM RADAR-CENTERED TO GEOCENTRIC CENTERED EQUATORIAL-POLAR FRAME

Target position coordinates in a radar-centered, right-handed equatorial-polar reference frame are translated to position coordinates in a geocentric right-handed equatorial-polar reference frame by simple vector addition.

$$E = E' + E'' \tag{C1}$$

$$F = F' + F'' \tag{C2}$$

$$G = G' + G'' \tag{C3}$$

where E', F', and G' are the position coordinates of the radar site in the spheroid-geocentric, equatorial-polar triad, and E", F", and G" are the target's radar-centered position coordinates alined with the equatorial-polar triad.

This relationship is shown pictorially in figure C-1.

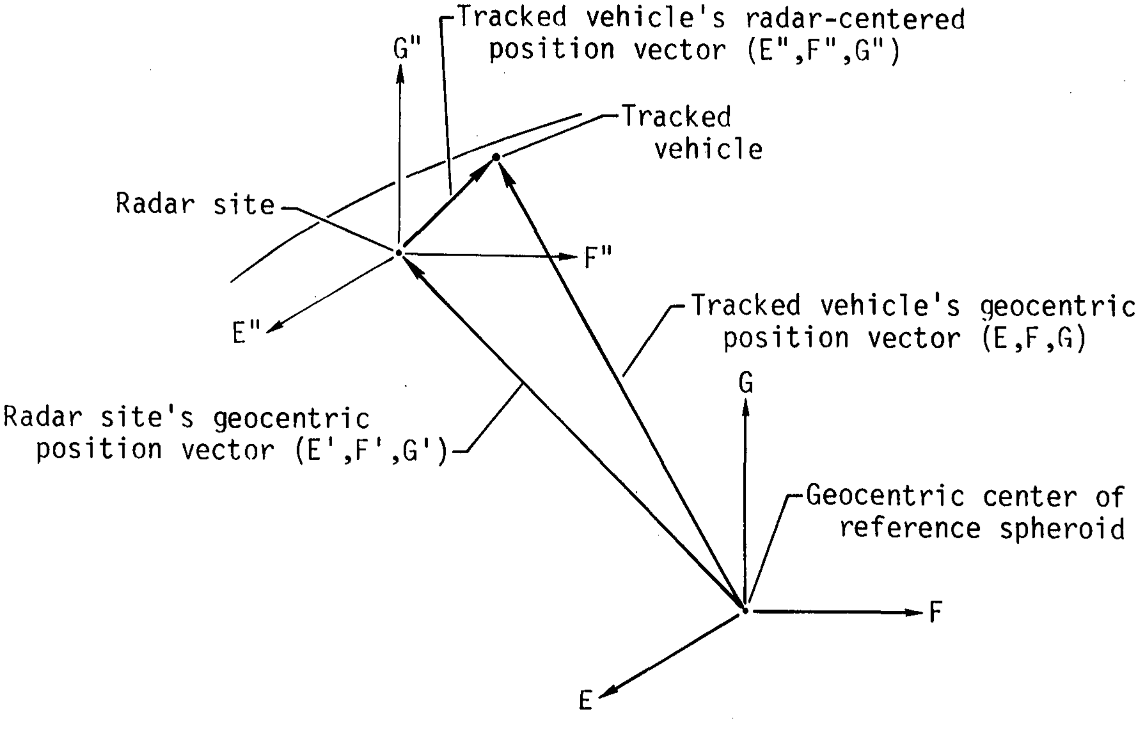

Figure C-1

APPENDIX D.--CONVERSION BETWEEN GEODETIC AND GEOCENTRIC LATITUDE FOR ON-SPHEROID POINTS

The equation for an ellipse in Cartesian coordinates is given by

$$\frac{x^2}{a^2} + \frac{y^2}{b^2} = 1 \tag{D1}$$

where a is the length of the semimajor axis and b is the length of the semiminor axis. The eccentricity, e, which is a measure of the flattening of the ellipse, is given by

$$e^2 = \frac{a^2 - b^2}{a^2} \tag{D2}$$

Combining (D1) and (D2) provides the equation for an ellipse in a slightly different form which is often useful in transformation relations,

$$x^2(1 - e^2) + y^2 = a(1 - e^2) \tag{D3}$$

Figure D-1 represents the first quadrant of a meridian ellipse with surface tangent line, MT, constructed at the point T. The geodetic latitude of the point T is given by U, and the geocentric latitude of the same point is given by U". The slope of the tangent line, obtained by differentiation of equation (D3), is given by

$$\frac{dy}{dx} = - \frac{x}{y}(1 - e^2) \tag{D4}$$

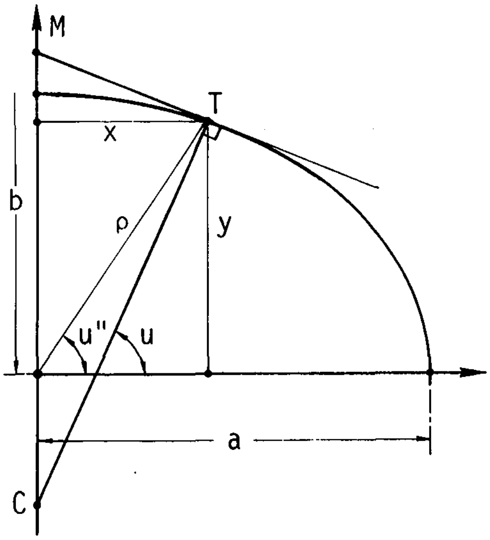

Figure D-1

The slope of the normal line, TC, is simply the negative of the same expression or

$$-\frac{dx}{dy} = \frac{y}{x(1 - e^2)} = \tan U \tag{D5}$$

From the geometry of figure D-1 it is apparent that values for x and y can be obtained as

$$x = \rho \cos U'' \quad \text{and} \quad y = \rho \sin U'' \tag{D6}$$

which can be substituted in equation (D5) to obtain the desired relationship between on-spheroid geodetic and geocentric latitude,

$$\tan U'' = (1 - e^2) \tan U \tag{D7}$$

APPENDIX E.--CALCULATION OF GEODETIC LATITUDE AND ALTITUDE OF AN OFF-SPHEROID TARGET FROM THE TARGET GEOCENTRIC RADIUS VECTOR

Calculation of geodetic latitude and altitude from a target's geocentric position vector is accomplished using the method of Purcell and Cowan (ref. 5). This method is based on the use of small angle approximations which enhance processing speed and which have a negligible effect on computational accuracy.

Figure E-1 represents the first quadrant of a meridian ellipse from an oblate earth of eccentricity, e. The position of the target is denoted by the point, P, at an altitude, h, above the surface of the reference spheroid. The target's geodetic latitude is denoted by U, its geocentric latitude is denoted by U', and the geocentric latitude of the surface point whose outward normal passes through the target is denoted by U". The magnitude of the geocentric position vector is denoted by R, the geocentric radius of the earth along the geocentric position vector is denoted by R", and the geodetic earth radius to the surface normal point is denoted by N. Other points of interest are a, the length of the semi-major axis of the ellipse; b, the length of the semi-minor axis of the ellipse; d, the distance along the X axis from the origin to the intersection of the normal line; and c, the distance measured along the normal line from the point of intersection of the X axis to the surface intersection. The difference between geodetic and geocentric latitude is denoted by α at the point Q, by α' at the point T, and by β at the point P.

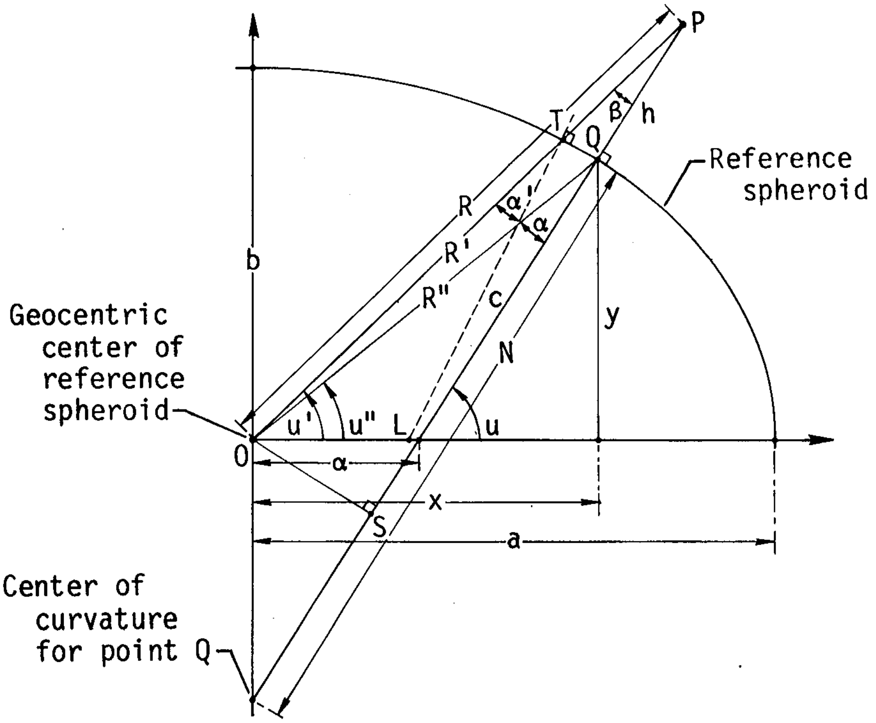

Figure E-1

It has been shown (app. D) that the relation between geodetic and geocentric latitude for on-spheroid points is given by

$$\tan U'' = (1 - e^2) \tan U \tag{E1}$$

Using double angle trigonometric relations it is possible to write

$$\tan (U - U'') = \frac{\tan U - \tan U''}{1 + \tan U \tan U''} \tag{E2}$$

in which the tan U" terms can be eliminated by the use of equation (E1) and α can be substituted for U - U" to yield

$$\tan \alpha = \frac{\tan U - (1 - e^2) \tan U}{1 + (1 - e^2) \tan^2 U} \tag{E3}$$

Equation (E3) can be further reduced to

$$\tan \alpha = \frac{e^2 \sin U \cos U}{1 - e^2 \sin^2 U} \tag{E4}$$

and since α is very small, tan α can be replaced by α to provide

$$\alpha = \frac{e^2 \sin U \cos U}{1 - e^2 \sin^2 U} \tag{E5}$$

A similar solution for α may be obtained in terms of U" by elimination of the tan U terms in equation (E2) in the same manner that the tan U" terms were eliminated in the above solution. This yields

$$\alpha = \frac{e^2 \sin U'' \cos U''}{1 - e^2 \sin^2 U} \tag{E6}$$

The difference between geodetic and geocentric latitude at point T may be determined by the same method, which yields

$$\alpha' = \frac{e^2 \sin U' \cos U'}{1 - e^2 \cos^2 U'} \tag{E7}$$

Again considering the geometry of the meridional ellipse shown in figure E-1, it can be seen that the angles α and α' appear very nearly equal. Although figure E-1 greatly exaggerates the ellipticity of the earth spheroid, the actual difference between the angles α and α' can be shown never to exceed 9×10^{-8} radians. Because of this, the convenient approximation can be made that

$$\alpha = \frac{e^2 \sin U' \cos U'}{1 - e^2 \cos^2 U'} \qquad \text{(E8)}$$

Next, an expression for R' may be simply obtained from the polar form of an equation for an ellipse as

$$R' = \frac{b}{(1 - e^2 \cos^2 U')^{1/2}} \qquad \text{(E9)}$$

Applying the law of sines to triangle OPL provides the relation

$$d = R \sin \beta/\sin U = R'' \sin \alpha/\sin U \qquad \text{(E10)}$$

from which

$$\sin \beta = \frac{R'' \sin \alpha}{R} \qquad \text{(E11)}$$

Again, since both α and α' and R' and R" differ only by a negligible amount, equation (E11) can be rewritten as

$$\sin \beta = \frac{R' \sin \alpha}{R} \qquad \text{(E12)}$$

without significant loss of accuracy. Finally, since both α' and β are very small, equation (E12) can be simplified to

$$\beta = R'\alpha/R \qquad \text{(E13)}$$

The final step in the calculation of geodetic latitude from the target's geocentric latitude is accomplished by noting in figure E-1 that

$$U = U' + \beta \qquad \text{(E14)}$$

Thus, the transformation from geocentric to geodetic latitude can be accomplished by:

1. Calculation of the angle α using eccentricity, e, and geocentric latitude, U' (eq. (E8))

2. Calculation of R' using eccentricity, e, and geocentric latitude, U' (eq. (E9)).

3. Calculation of α and β from R' (eq. (E13))

4. Calculation of geodetic latitude, U, from geocentric latitude, U', and β (eq. (E14))

It now remains to calculate the altitude of the target above the reference spheroid. Although the difference between R' and R" does not have appreciable effect on the calculation of α, it can introduce measurable error in the calculation of h. Therefore, it is desirable to obtain a more accurate solution for h than would be possible by direct substitution. This is accomplished by obtaining a relationship between h and the known parameters R, R', α', and β.

From the equation of an ellipse in polar form the ratio between R" and R' can be expressed as

$$\frac{R''}{R'} = \frac{(1 - e \cos U')^{1/2}}{(1 - e^2 \cos^2 U'')^{1/2}} \tag{E15}$$

which may be rewritten as

$$\frac{R''}{R'} = \left[\frac{1 - e^2 \cos^2 U''}{1 - e^2 \cos^2 U''} + \frac{e^2 \cos^2 U'' - e^2 \cos^2 U'}{1 - e^2 \cos^2 U''}\right]^{1/2} \tag{E16}$$

$$= \left[1 + \frac{e^2(\cos^2 U'' - \cos^2 U)}{1 - e^2 \cos^2 U''}\right]^{1/2} \tag{E17}$$

$$= \left[1 + \frac{e^2[\sin(U'' + U') \sin(U' - U'')]}{1 - e^2 \cos^2 U''}\right]^{1/2} \tag{E18}$$

$$= \left[1 + \frac{e^2(\sin U'' \cos U' + \cos U'' \sin U')}{1 - e^2 \cos^2 U''} \sin(U' - U'')\right]^{1/2} \tag{E19}$$

From figure E-1 it is apparent that U' - U" = β - α' is a very small angle. This allows another convenient approximation to be made. That is, sin U' is approximately equal to sin U", and cos U' is approximately equal to cos U". Thus, by substituting β - α' for U' - U", by using the sine and cosine approximations, and by combining equations (E8) and (E19), the R"/R' ratio may now be written as

$$\frac{R''}{R'} = \left[1 + \frac{1 + 2 e^2 \sin U' \cos U'}{1 - e^2 \sin^2 U'} (\beta - \alpha)\right]^{1/2} \tag{E20}$$

or

$$\frac{R''}{R'} = [1 + 2\alpha(\alpha - \beta)]^{1/2} \tag{E21}$$

Substituting the value for β obtained from equation (E13) yields

$$\frac{R''}{R'} = 1 + 2\alpha'(1 - R''/R)^{1/2} \tag{E22}$$

Applying the first two terms of the binomial expansion to equation (E22) yields

$$\frac{R''}{R'} = 1 + \frac{\alpha'^2}{R}(R - R'') \tag{E23}$$

Noting that R - R" very nearly equals h, and making the substitution

$$R'' - R' = \alpha'\beta h \tag{E24}$$

a value for R" can be obtained as

$$R'' = R' + \alpha'\beta h \tag{E25}$$

Applying trigonometric relations to triangles OPS and OQS in figure E-1, an expression for h can be written as

$$h = R \cos \beta - R'' \cos \alpha' \tag{E26}$$

Approximating cos α and cos β with the first two terms of a cosine series, equation E26 becomes

$$h = R(1 - \beta^2/2) - R''(1 - \alpha'^2/2) \tag{E27}$$

or

$$h = (R - R'') - \frac{1}{2}(R\beta^2 - R''\alpha'^2) \tag{E28}$$

Noting that (eq. (E13)) $\alpha' = \beta(R/R'')$ and $\beta = \alpha'(R''/R)$, equation (E28) can be rewritten

$$h = (R - R'') - \frac{1}{2}(R''\alpha'\beta - R\alpha'\beta) \tag{E29}$$

or with further reduction

$$h = (R - R'')(1 + \alpha'\beta/2) \tag{E30}$$

It now remains to combine equations (E25) and (E30) to obtain an expression for h in terms of R, R', α', and β as

$$h = [R - (\alpha'\beta h + R')](1 + \alpha'\beta/2) \tag{E31}$$

Multiplying the two right-hand terms and rearranging, this becomes

$$h = \frac{(R - R')(1 + \alpha'\beta/2)}{1 + \alpha'\beta + \alpha'^2\beta^2/2} \tag{E32}$$

Since the second term in the numerator is simply the first two terms of the expansion of $(1 - \alpha'\beta/2)^{-1}$ and since the denominator is nearly the value of the first three terms of the expansion of $(1 - \alpha'\beta/2)^{-2}$, equation (E31) can be simplified to

$$h = \frac{(R - R')(1 - \alpha'\beta/2)^{-1}}{(1 - \alpha'\beta/2)^{-2}} \tag{E33}$$

which upon cancellation becomes

$$h = (R - R')(1 - \alpha'\beta/2) \tag{E34}$$

Table E1 compares the results of the Purcell and Cowan method with exact values for both target altitude and geodetic latitude for several representative points. The surface error represents the horizontal distance between the exact latitude and the computed latitude as would be measured on the surface of the reference spheroid. For targets at an altitude of 1000 meters above the reference spheroid, the horizontal error is on the order of ±0.01 meter or less; for targets at 10,000 meters, the error is on the order of ±0.1 meter or less; and for targets at 1×10^6 meters, the error is on the order of ±1.0 meter or less. The error in the altitude computation is insignificant for targets at any altitude. The maximum altitude error in table E1 is found to be only ±0.0003 meter with root-mean-squared errors being less than ±0.0001 meter.

Thus, it is possible to determine the geodetic latitude and altitude of a target using the target's geocentric radius vector by the use of equations (E8), (E9), (E13), (E14), and (E34). Although a number of approximations are used in the calculations, comparisons of the results of this method with those of the Lagrange multiplier method (ref. 6), which uses a closed form solution with no approximations, shows that the results are accurate well beyond the range and angle resolution of present tracking equipment. Furthermore, the speed enhancement obtained through the use of the Purcell and Cowan method permits the solution to be used in real-time applications where a large number of additional computations must be performed.

TABLE E1.--COMPARISON OF LATITUDE AND ALTITUDE COMPUTATIONS WITH EXACT VALUES FOR THE SAME PARAMETERS

Exact latitude, deg	Computed latitude, deg	Surface error, m	Exact altitude, m	Computed altitude, m	Altitude error, m
0.0000000000	0.0000000000	0.000	1000.0000	1000.0000	0.0000
0.0000000000	0.0000000000	0.000	10000.0000	10000.0000	0.0000
0.0000000000	0.0000000000	0.000	100000.0000	100000.0000	0.0000
10.0000000000	10.0000000975	0.011	1000.0000	999.9998	0.0002
10.0000000000	10.0000006941	0.077	10000.0000	9999.9997	0.0003
10.0000000000	10.0000064877	0.722	100000.0000	99999.9997	0.0003
20.0000000000	20.0000002992	0.033	1000.0000	1000.0001	-0.0001
20.0000000000	20.0000012156	0.135	10000.0000	10000.0000	0.0000
20.0000000000	20.0000100990	1.125	100000.0000	100000.0000	0.0000
30.0000000000	30.0000005731	0.064	1000.0000	1000.0002	-0.0002
30.0000000000	30.0000013810	0.154	10000.0000	10000.0002	-0.0002
30.0000000000	30.0000092079	1.026	100000.0000	100000.0001	-0.0001
40.0000000000	40.0000007485	0.083	1000.0000	999.9999	0.0001
40.0000000000	40.0000010705	0.119	10000.0000	9999.9999	0.0001
40.0000000000	40.0000041834	0.466	100000.0000	99999.9999	0.0001
50.0000000000	50.0000006805	0.076	1000.0000	1000.0000	0.0000
50.0000000000	50.0000003653	0.041	10000.0000	10000.0000	0.0000
50.0000000000	49.9999973061	0.300	100000.0000	100000.0000	0.0000
60.0000000000	60.0000003982	0.044	1000.0000	1000.0001	-0.0001
60.0000000000	59.9999995932	0.045	10000.0000	10000.0001	-0.0001
60.0000000000	59.9999917913	0.916	100000.0000	100000.0001	-0.0001
70.0000000000	70.0000000974	0.011	1000.0000	1000.0000	0.0000
70.0000000000	69.9999991813	0.091	10000.0000	10000.0000	0.0000
70.0000000000	69.9999902906	1.084	100000.0000	100000.0001	-0.0001
80.0000000000	79.9999999628	0.004	1000.0000	999.9999	0.0001
80.0000000000	79.9999993640	0.071	10000.0000	10000.0000	0.0000
80.0000000000	79.9999935553	0.720	100000.0000	100000.0000	0.0000
90.0000000000	90.0000000000	0.000	1000.0000	1000.0000	0.0000
90.0000000000	90.0000000000	0.000	10000.0000	10000.0000	0.0000
90.0000000000	90.0000000000	0.000	100000.0000	100000.0000	0.0000

APPENDIX F.--ROTATION OF RADAR POSITION VECTOR FROM TARGET-CENTERED, EQUATORIAL-POLAR ALINEMENT INTO TARGET-CENTERED, EAST-NORTH-VERTICAL ALINEMENT

Radar position given in terms of a target-centered, equatorial-polar alined reference frame may be converted to target-centered east-north-vertical coordinates by the use of a standard matrix relation:

$$\begin{bmatrix} X \\ Y \\ Z \end{bmatrix} = \begin{bmatrix} \sin W & \cos W & 0 \\ -\cos W \sin U & \sin W \sin U & \cos U \\ \cos W \cos U & -\sin W \cos U & \sin U \end{bmatrix} \begin{bmatrix} E'' \\ F'' \\ G'' \end{bmatrix} \qquad \text{(F1)}$$

where U and W represent the geodetic latitude and longitude of the target vehicle; where E", F", and G" represent the radar's Cartesian coordinates referenced to a target-centered, equatorial-polar coordinate frame; and where X, Y, and Z represent the radar's position coordinates in a target-centered east-north-vertical reference frame.

Figure F-1 is a superposition of the radar's position coordinates in the two target-centered reference frames.

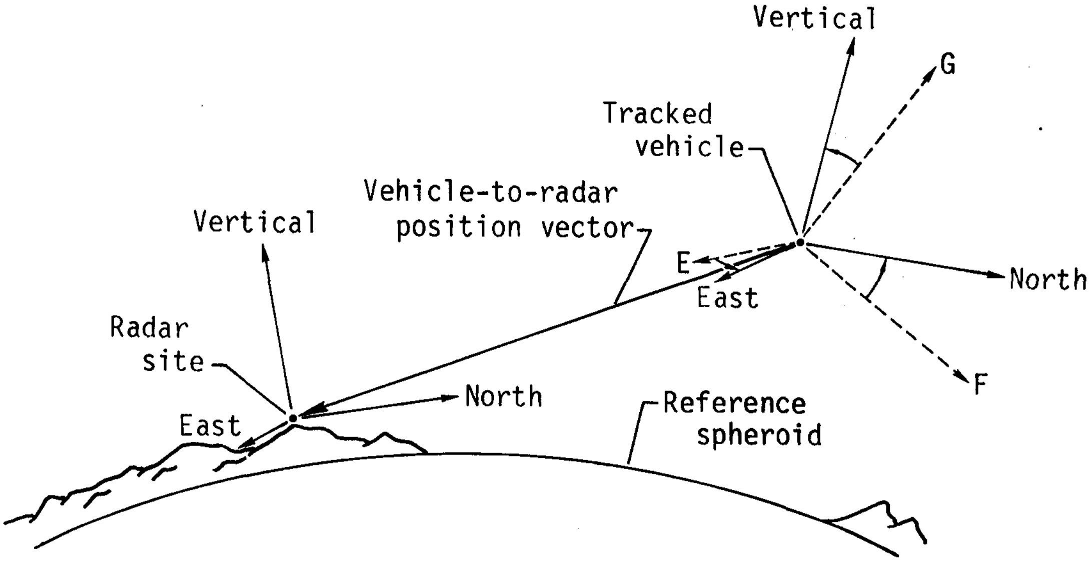

Figure F-1

APPENDIX G.--ROTATION OF RADAR POSITION VECTOR FROM TARGET-CENTERED, EAST-NORTH-VERTICAL ALINEMENT TO TARGET-CENTERED, BODY-AXIS ALINEMENT

To obtain the location of the impinging rf energy with respect to the target vehicle's body-axis triad, the radar position coordinates in a target-centered, east-north-vertical reference frame must be rotated to a target-centered, body-axis alined reference frame. This is accomplished by rotations through the roll (R), pitch (P), and heading (H) angles of the target vehicle. For this analysis the pitch angle was measured positive for nose up, the roll angle was measured positive for right wing down, and the heading angle was measured positive clockwise from north.

The rotation matrix is

$$A_{jk} = \begin{bmatrix} \cos P \cos H & -\cos P \sin H & \sin P \\ \sin R \sin P \cos H + \cos R \sin P & -\sin R \sin P \sin H + \cos R \cos P & -\sin R \cos P \\ -\cos R \sin P \cos H + \sin R \sin P & \cos R \sin P \sin H + \sin R \cos P & \cos R \cos P \end{bmatrix} \qquad \text{(G1)}$$

It is then possible to find the Cartesian elements of the radar position vector with respect to the target vehicle's body axes from

$$x_j = \sum_{k=1}^{3} A_{jk}\bar{x}_k (j = 1, 2, 3) \qquad \text{(G2)}$$

where $\bar{x}_k$ represents the kth position coordinates in the unrotated system and x_j represents the jth position coordinates in the rotated system. A more simplified expression for equation (G2) can be obtained by letting

$$\bar{X} = (\bar{x}_1, \bar{x}_2, \bar{x}_3) \qquad \text{(G3)}$$

and

$$A = A_{jk} = \begin{bmatrix} A_{11} & A_{12} & A_{13} \\ A_{21} & A_{22} & A_{23} \\ A_{31} & A_{32} & A_{33} \end{bmatrix} \qquad \text{(G4)}$$

from which equation (G2) may be rewritten as

$$X = A\bar{X} \qquad \text{(G5)}$$

REFERENCES

1. Loh, Yin-Chung; and Porter, James A.: RF Coverage Analysis and Performance for Shuttle Communication Links. IEEE Transactions on Communications, vol. Com-26, no. 11, Nov. 1978.

2. Berkowitz, Raymond S., ed.: Modern Radar. John Wiley & Sons, Inc., c.1965.

3. Skolnik, Merrill I., ed.: Radar Handbook. McGraw-Hill Book Co., c.1970.

4. Stratton, Julius A.: Electromagnetic Theory. McGraw-Hill Book Co., c.1941.

5. Purcell, E. W.; and Cowan, W. B.: Relating Geodetic Latitude and Altitude to Geocentric Latitude and Radius Vector. ARS, July 1961, pp. 932-934.

6. Hedgley, David R., Jr.: An Exact Transformation From Geocentric to Geodetic Coordinates for Nonzero Altitudes. NASA TR R-458, 1976.

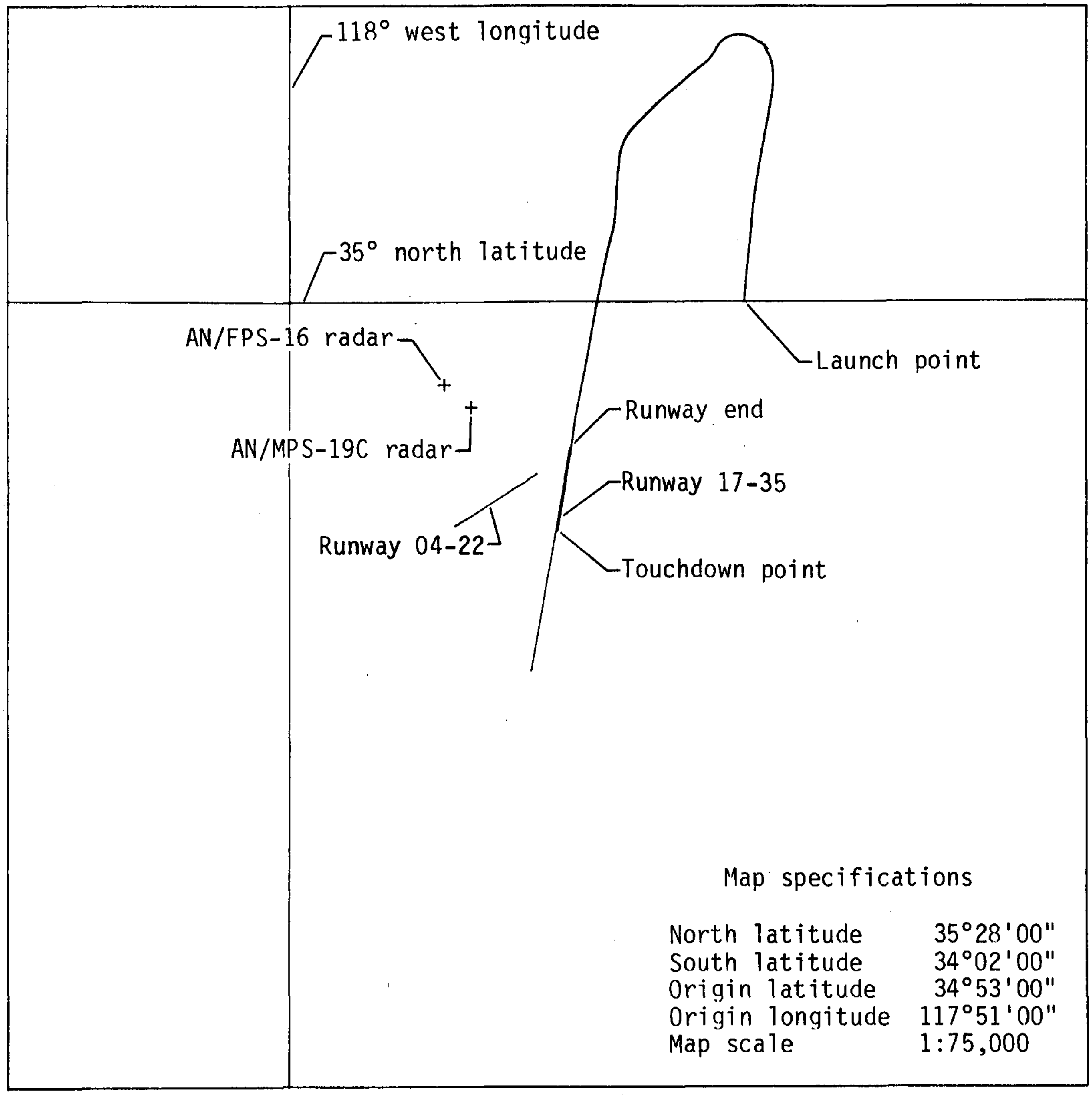

Map specifications

North latitude	35°28'00"
South latitude	34°02'00"
Origin latitude	34°53'00"
Origin longitude	117°51'00"
Map scale	1:75,000

Figure 1. Plot of AN/FPS-16 tracking data from launch to touchdown.

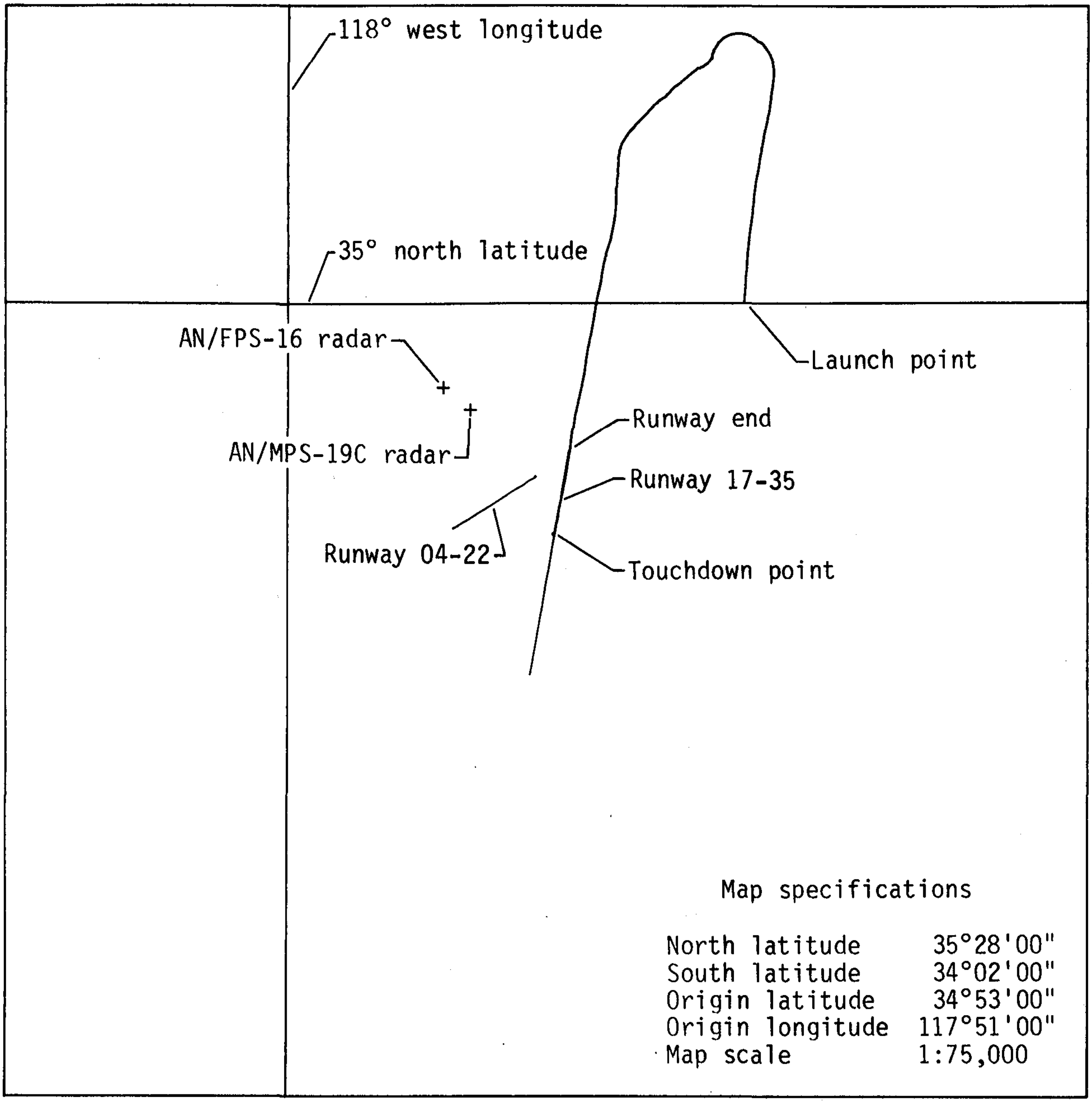

Figure 2. Plot of AN/MPS-19C tracking data from launch to touchdown.

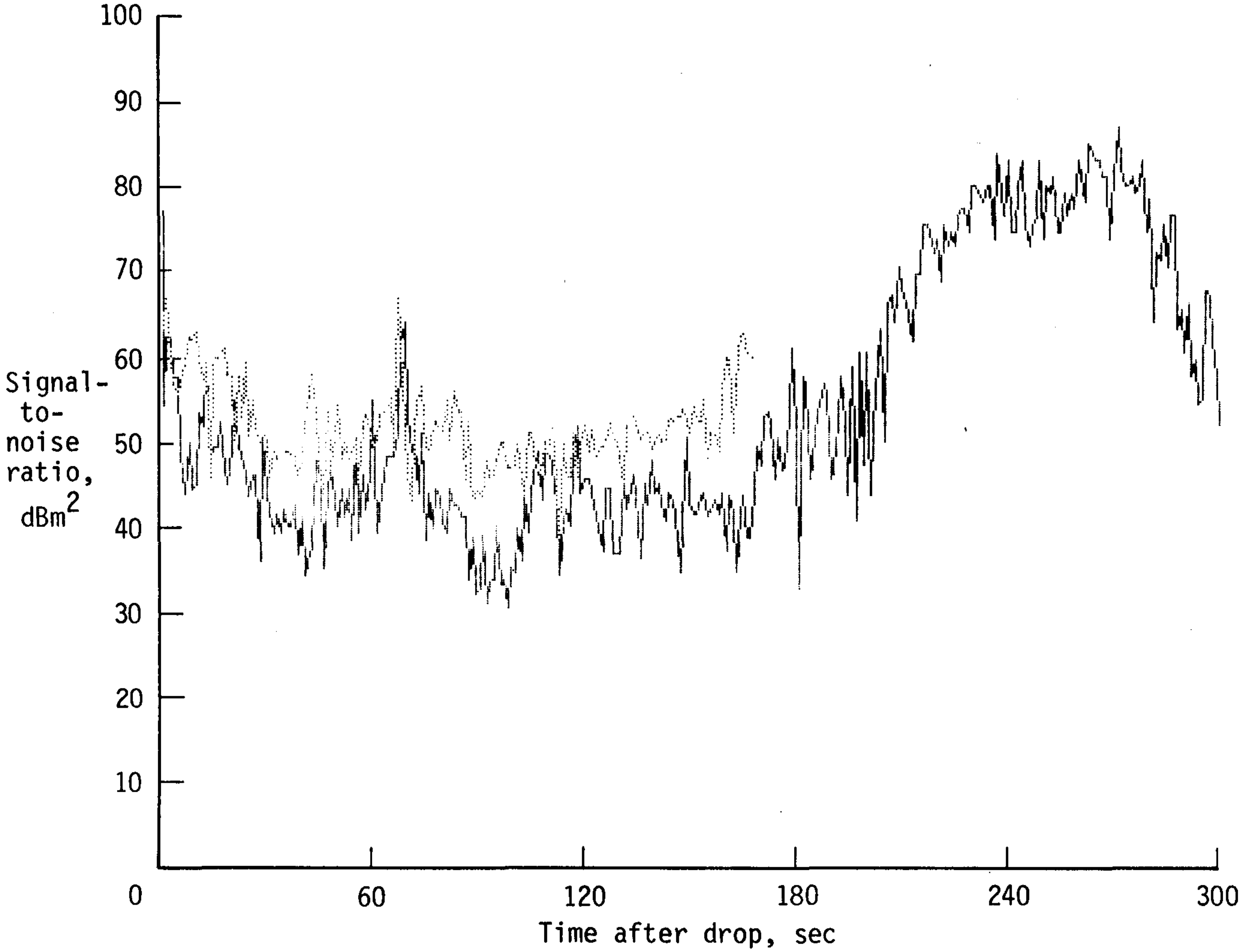

Figure 3. Signal-to-noise values during orbiter free flight measured at DFRC AN/FPS-16 and AN/MPS-19C radars. AN/FPS-16 data are shown as dotted line.

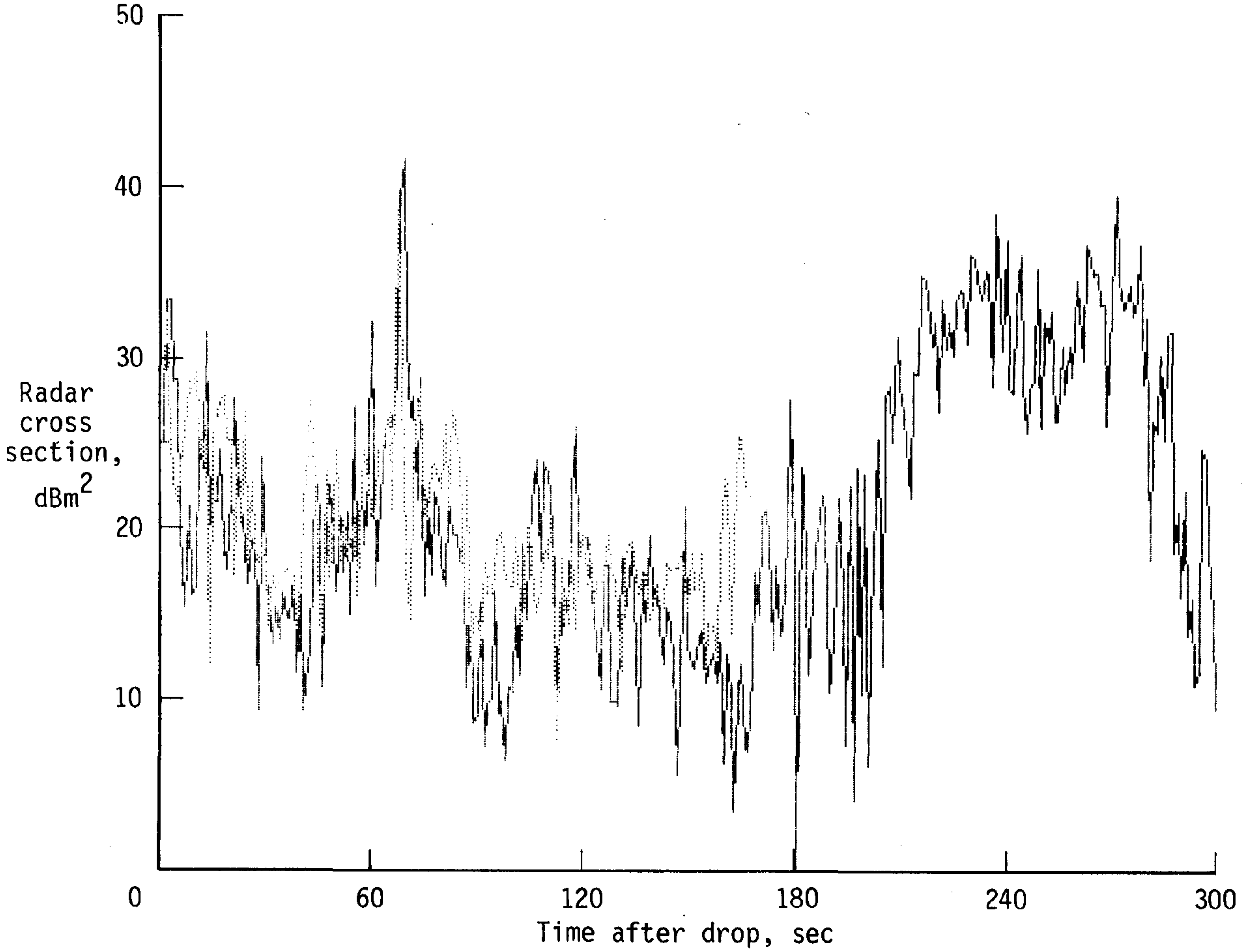

Figure 4. Radar cross section plotted as function of time after drop as computed from AN/FPS-16 and AN/MPS-19C data. AN/FPS-16 data are shown as dotted line.

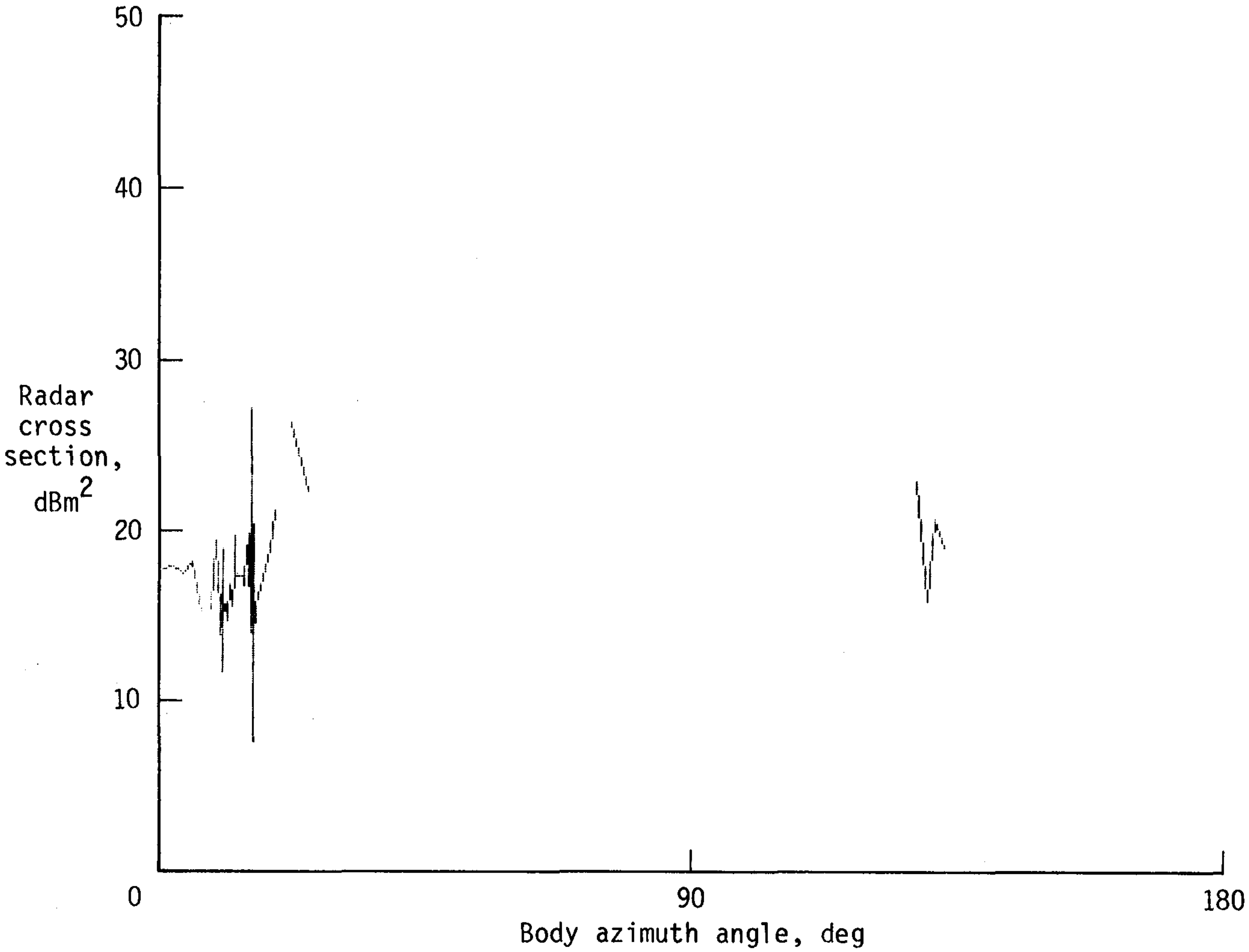

(a) Elevation aspect angle 0°, elevation window ±10°.

Figure 5. Radar cross section plotted as a function of body azimuth angle using AN/FPS-16 radar data.

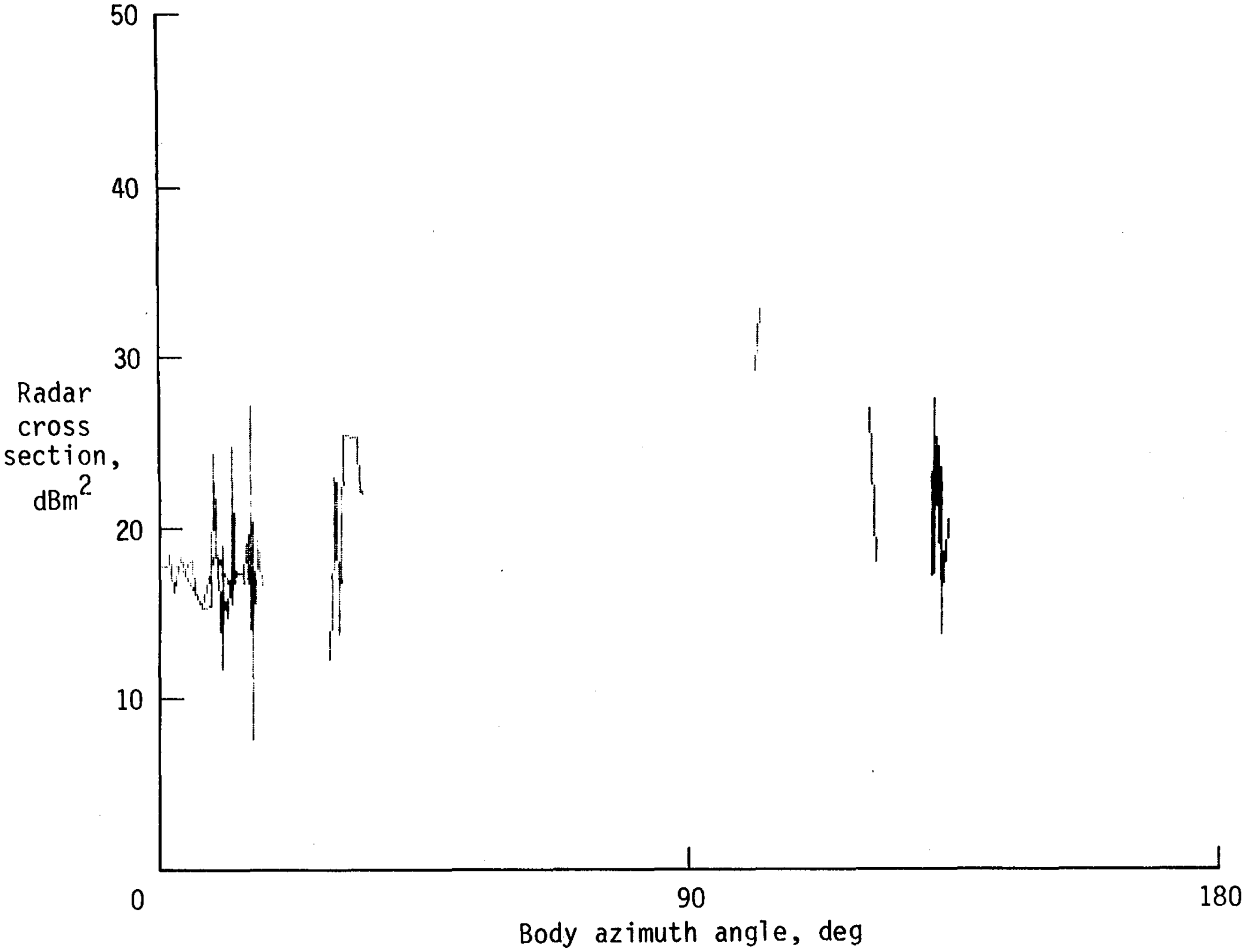

(b) Elevation aspect angle -10°, elevation window ±10°.

Figure 5. Continued.

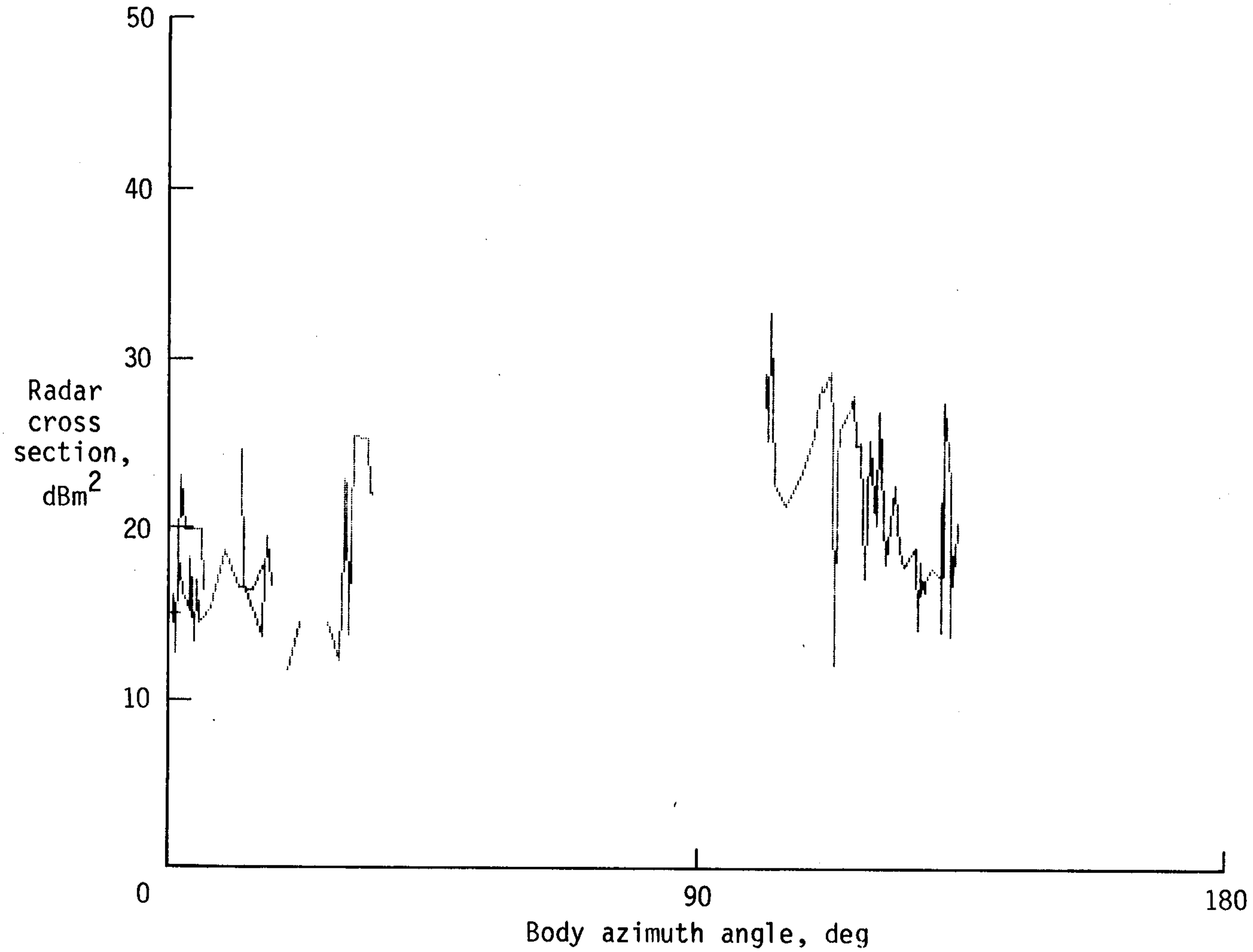

(c) Elevation aspect angle -20°, elevation window ±10°.

Figure 5. Continued.

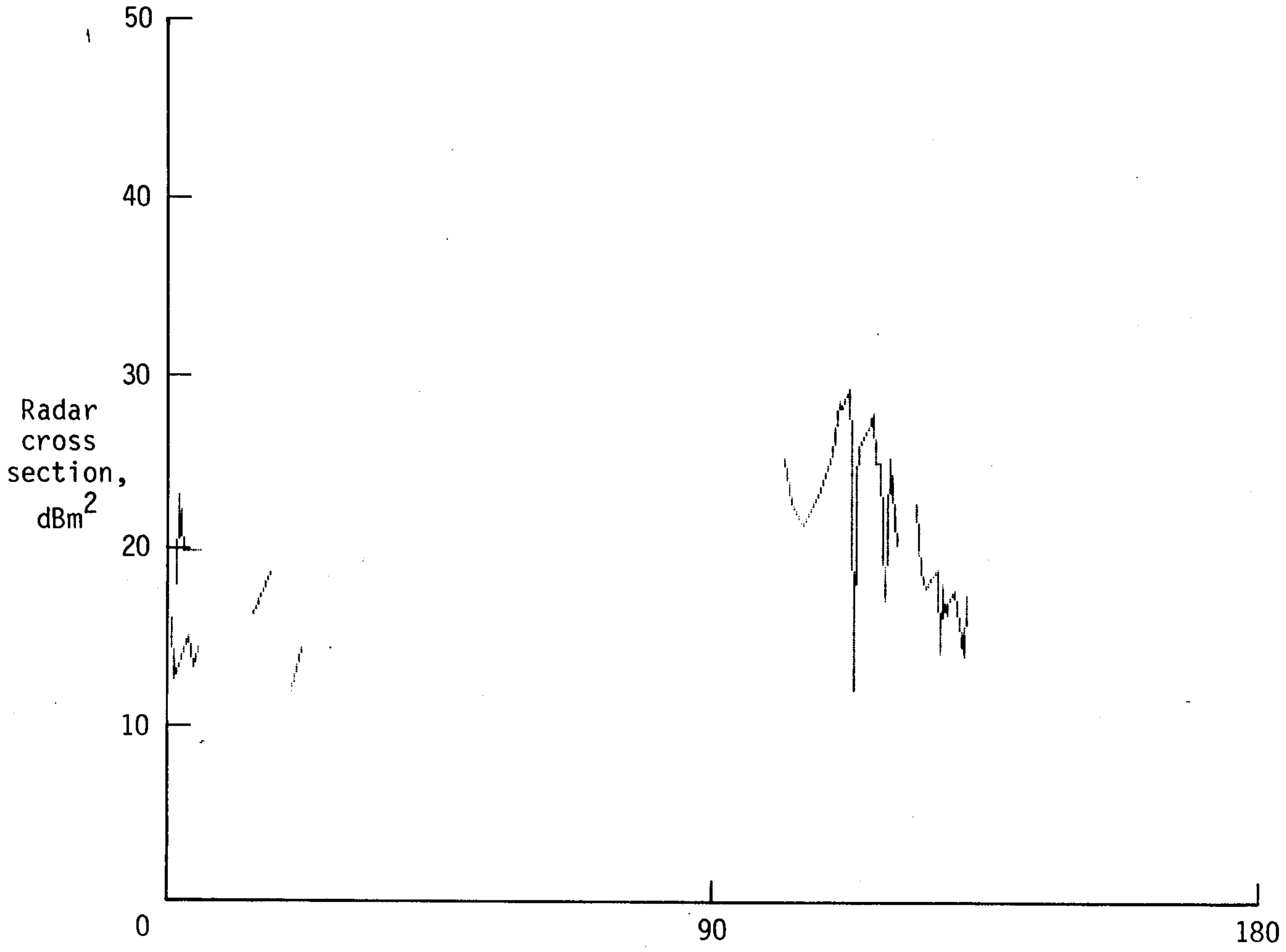

(d) Elevation aspect angle -30°, elevation window ±10°.

Figure 5. Concluded.

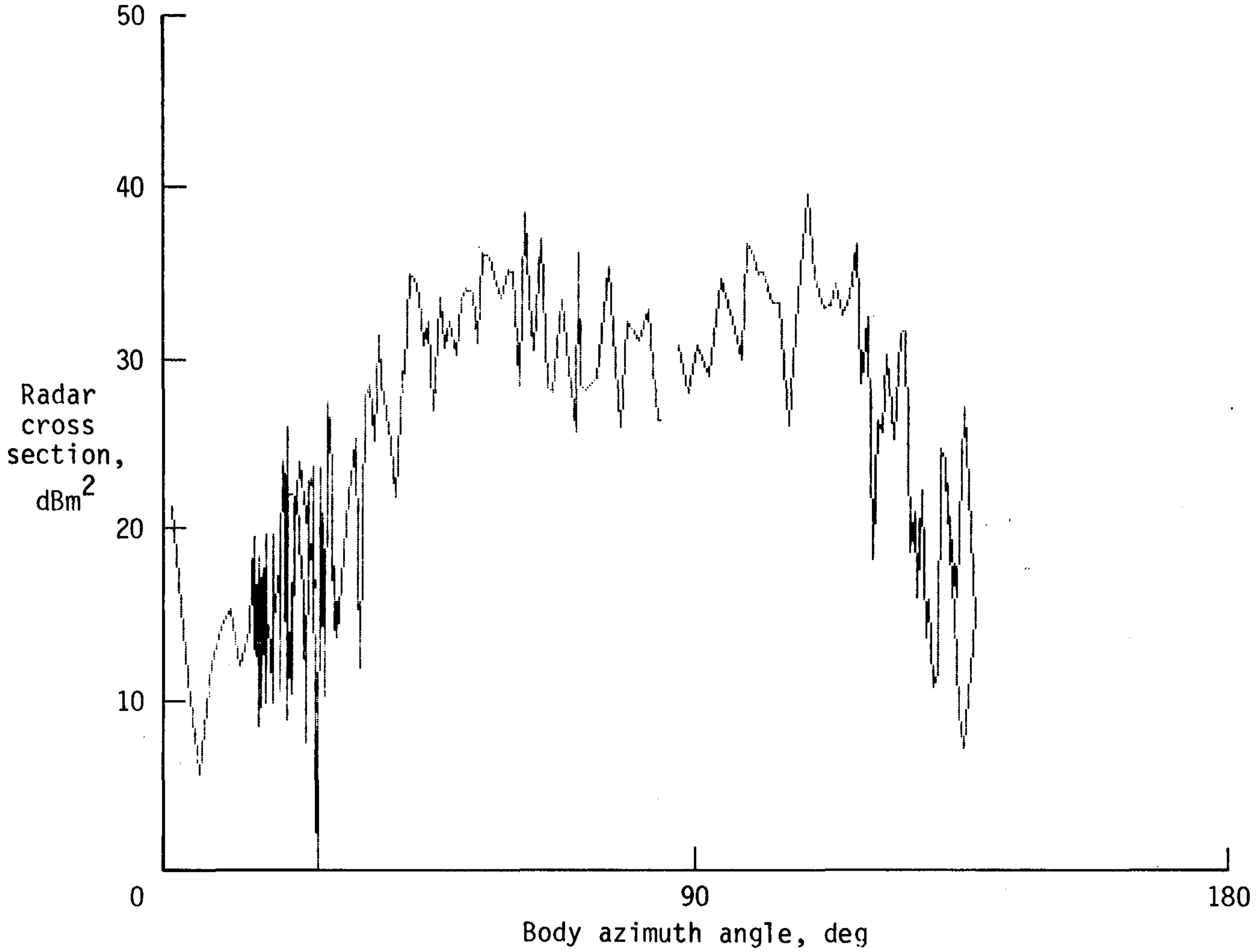

(a) Elevation aspect angle 0°, elevation window ±10°.

Figure 6. Radar cross section plotted as a function of body azimuth angle using AN/MPS-19C radar data.

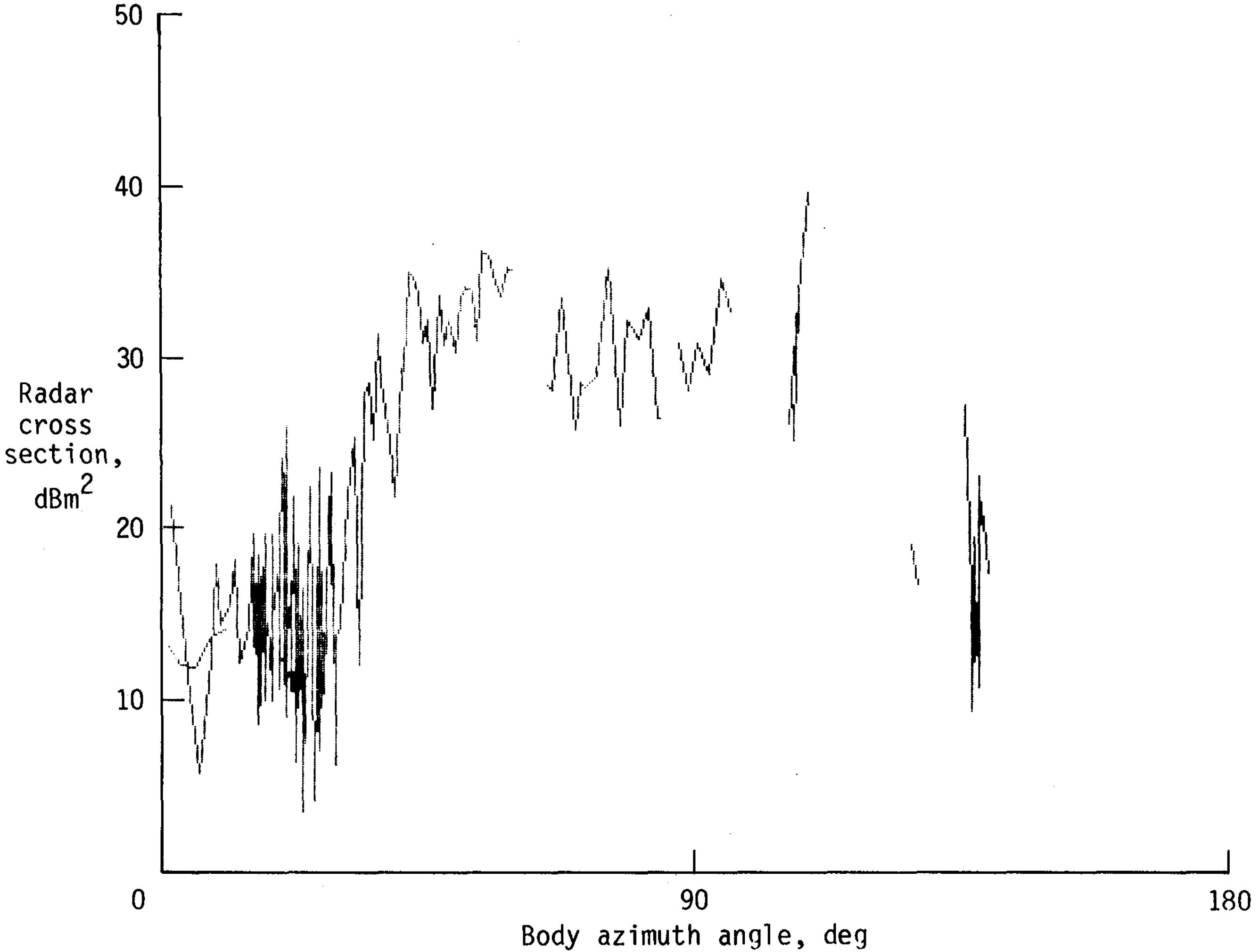

(b) Elevation aspect angle -10°, elevation window ±10°.

Figure 6. Continued.

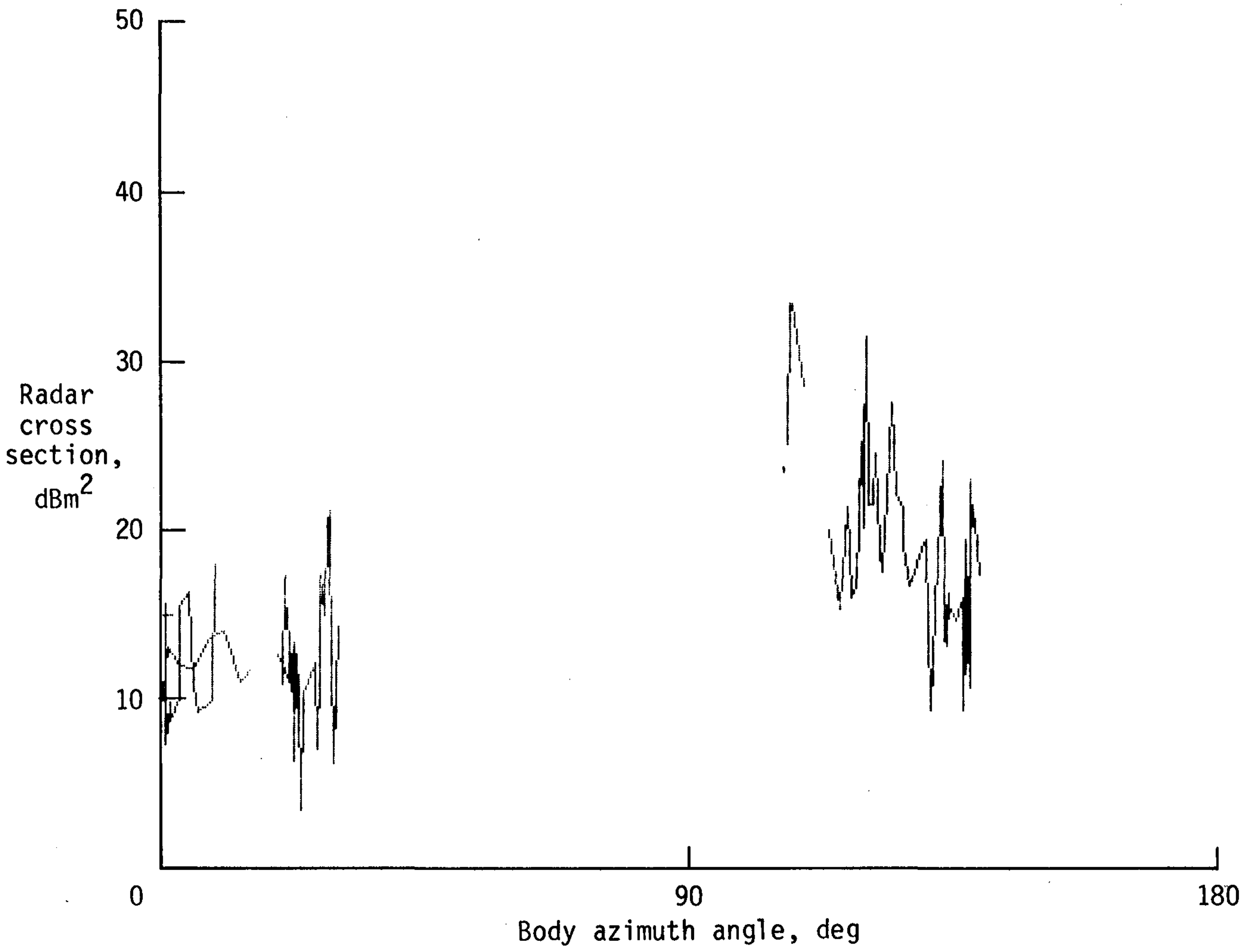

(c) Elevation aspect angle -20°, elevation window ±10°.

Figure 6. Continued.

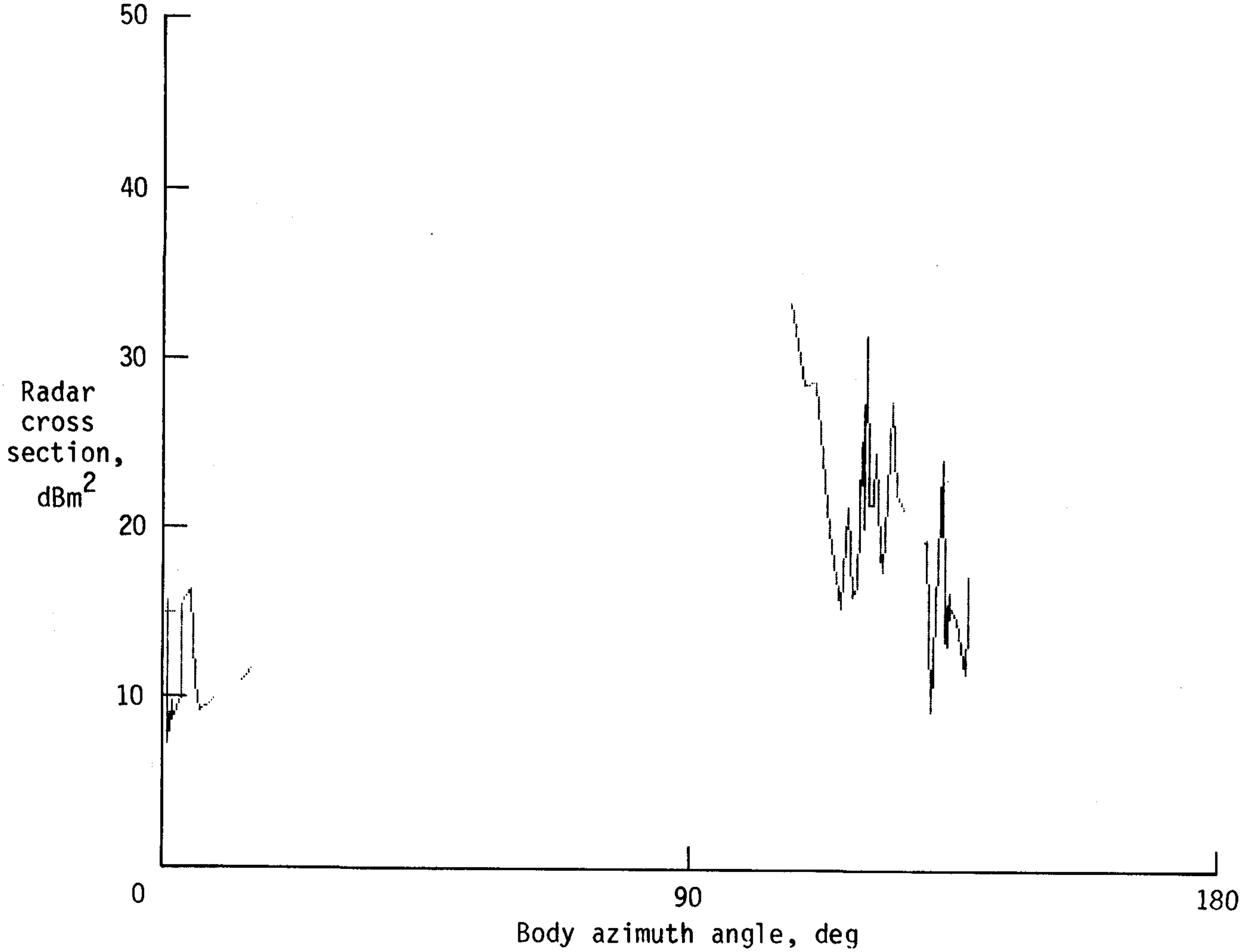

(d) Elevation aspect angle -30°, elevation window ±10°.

Figure 6. Concluded.

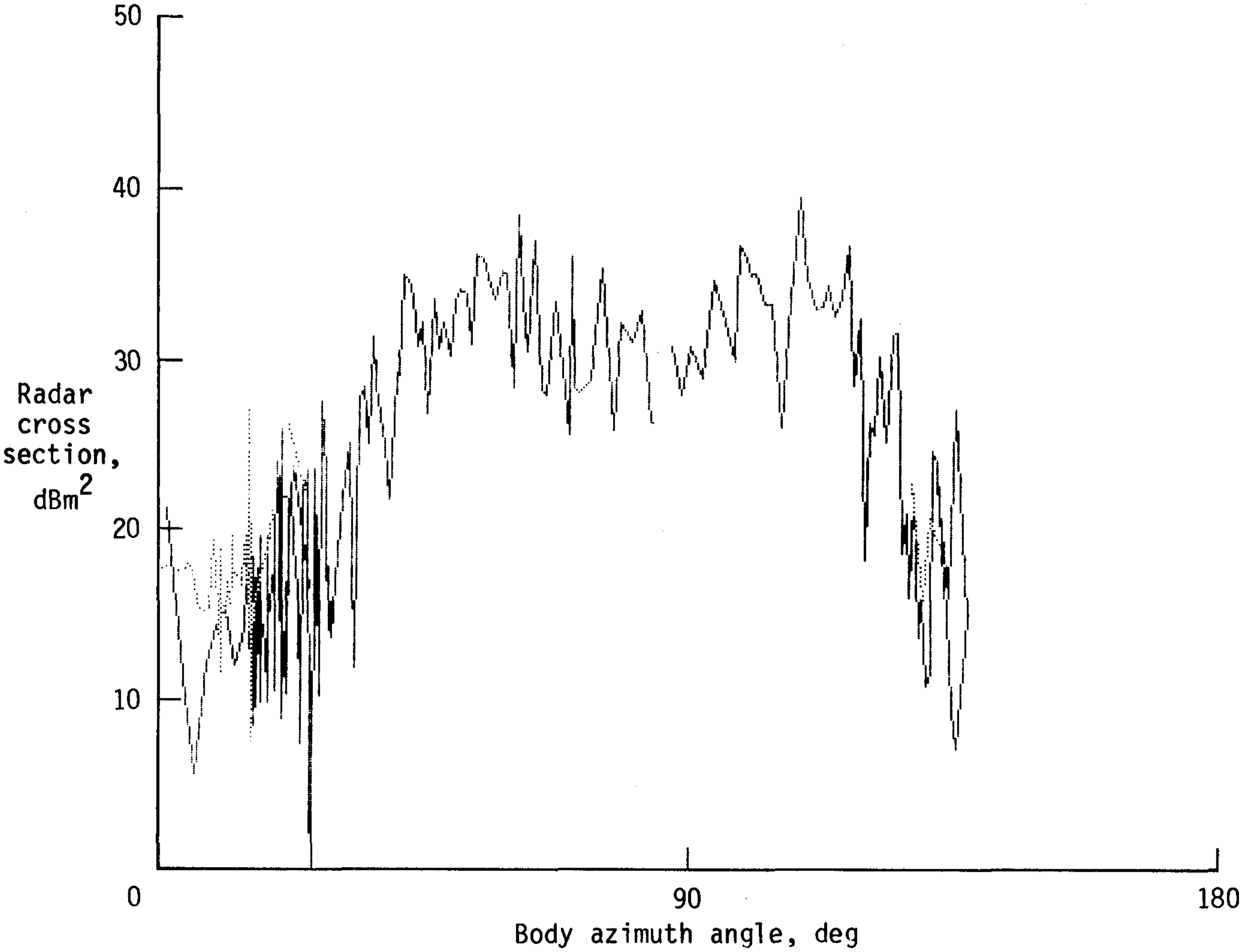

(a) Elevation aspect angle 0°, elevation window ±10°.

Figure 7. Radar cross section plotted as a function of body azimuth angle using AN/FPS-16 and AN/MPS-19C radar data. AN/FPS-16 data are shown as dotted line.

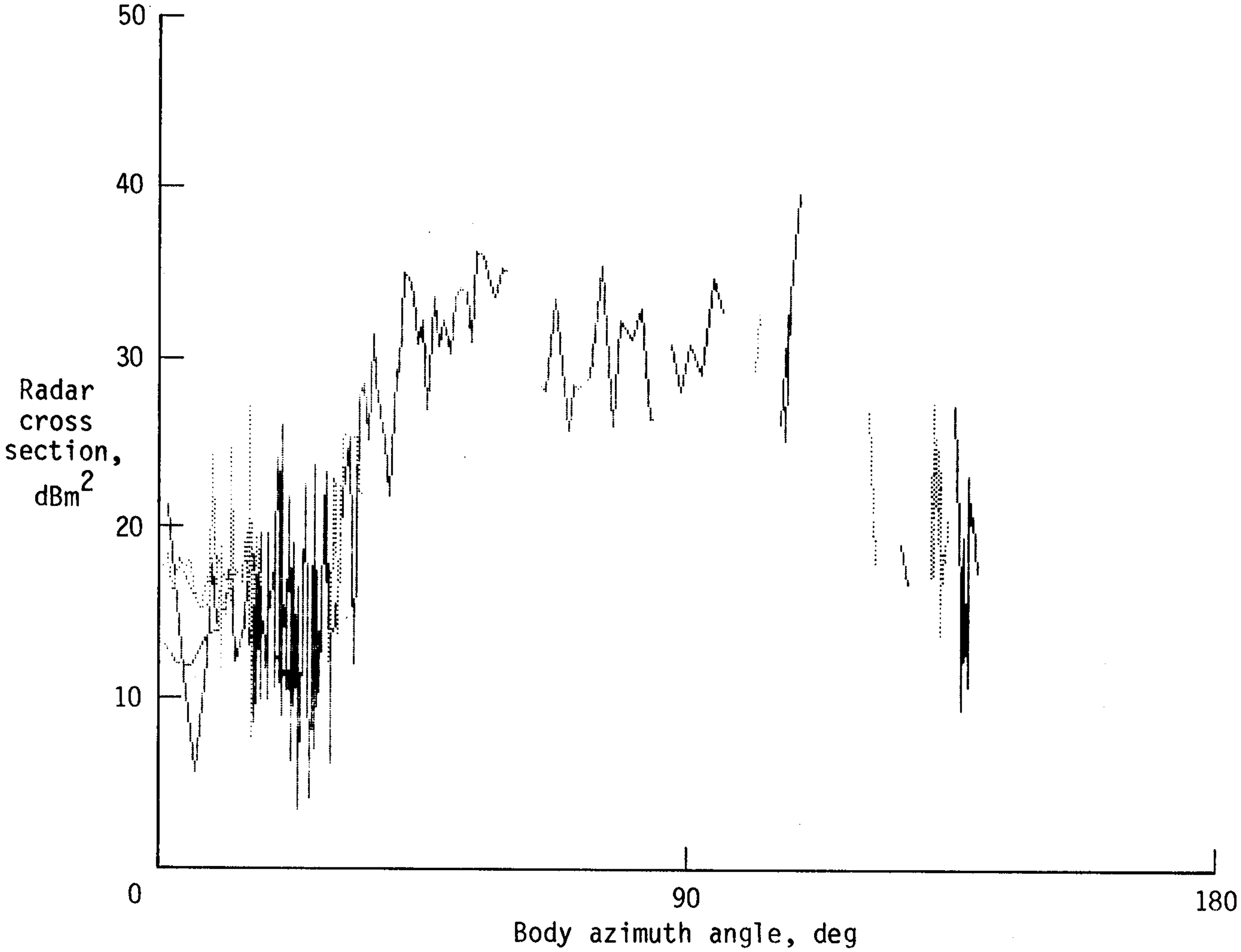

(b) Elevation aspect angle -10°, elevation window ±10°.

Figure 7. Continued.

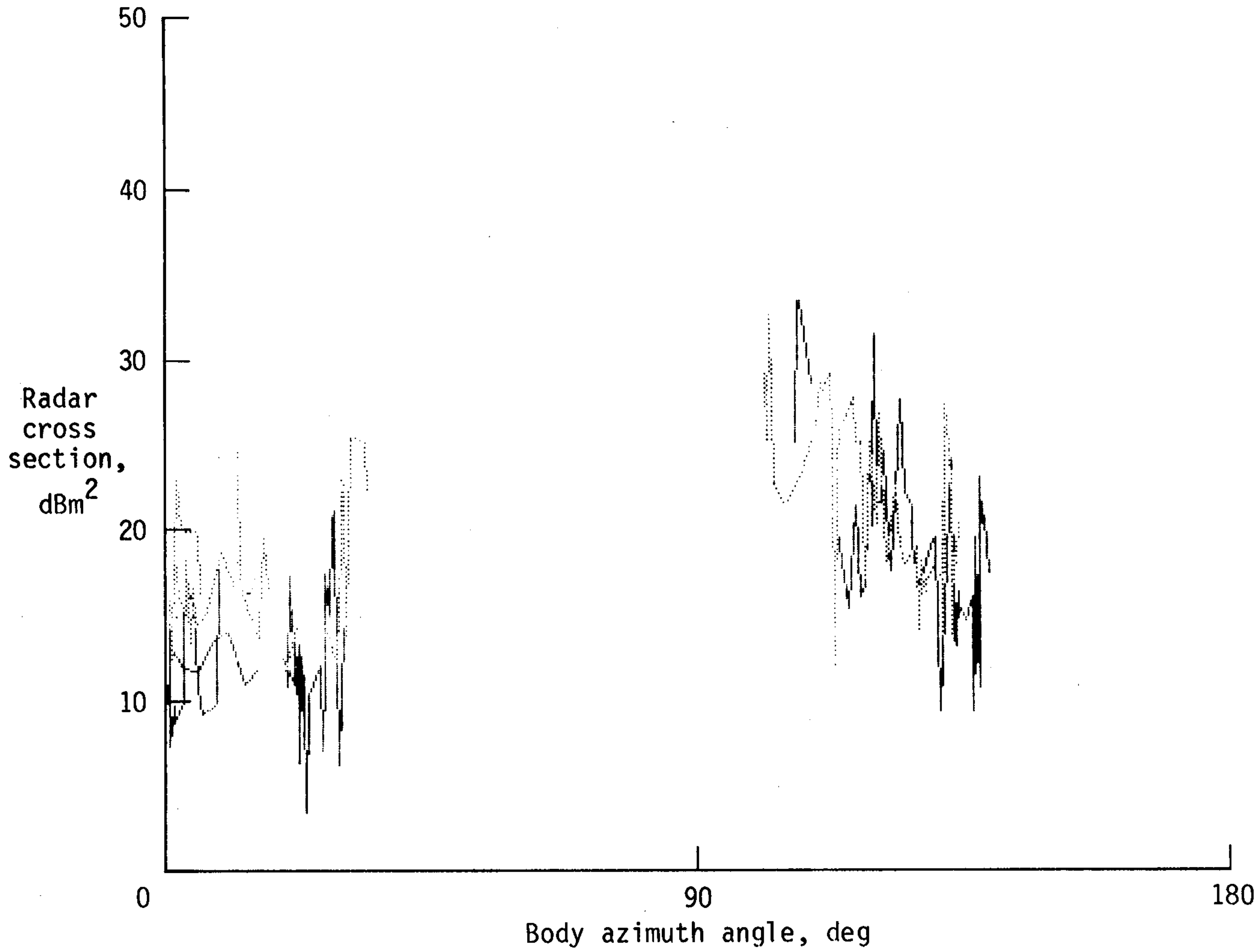

(c) Elevation aspect angle -20°, elevation window ±10°.

Figure 7. Continued.

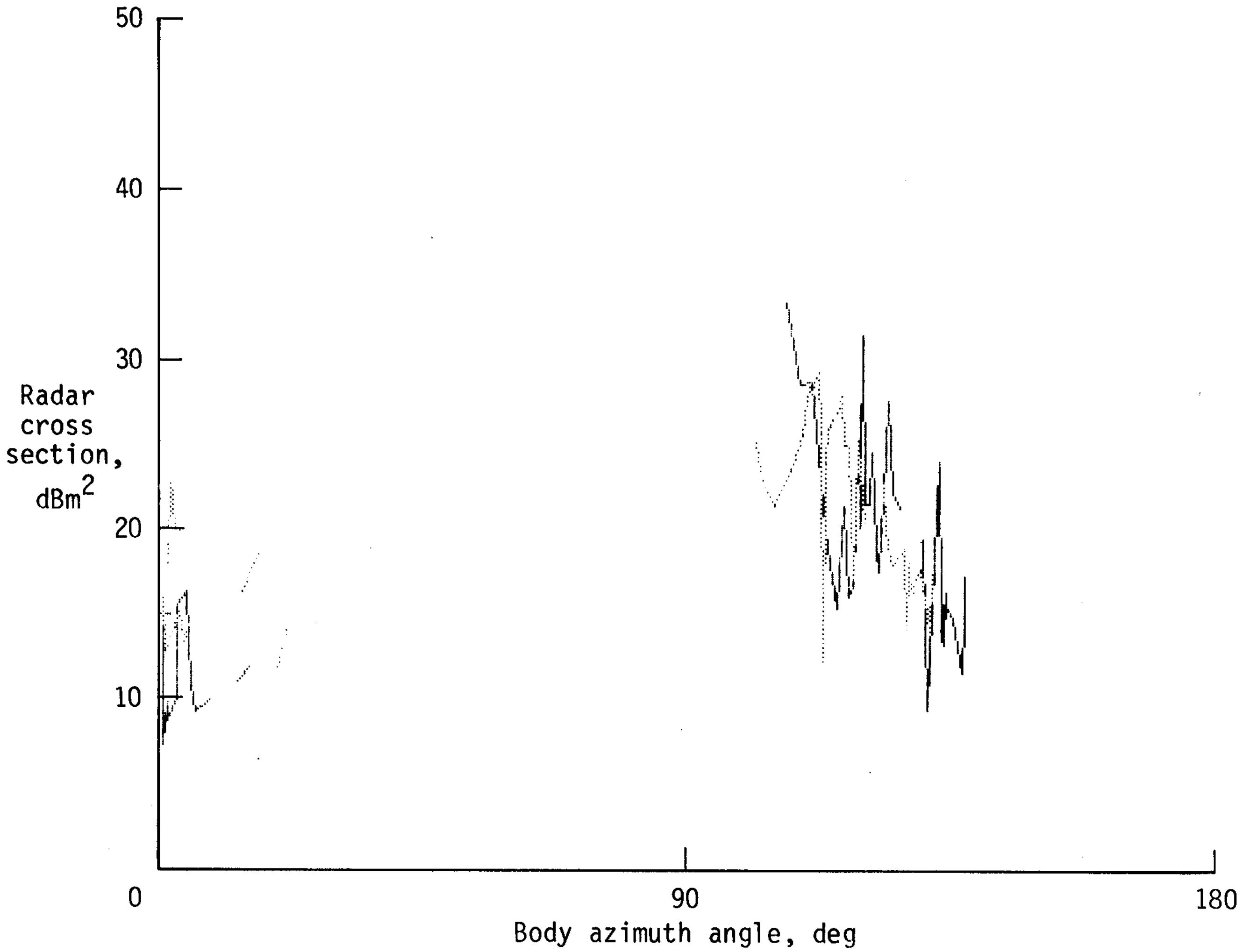

(d) Elevation aspect angle -30°, elevation window ±10°.

Figure 7. Concluded.

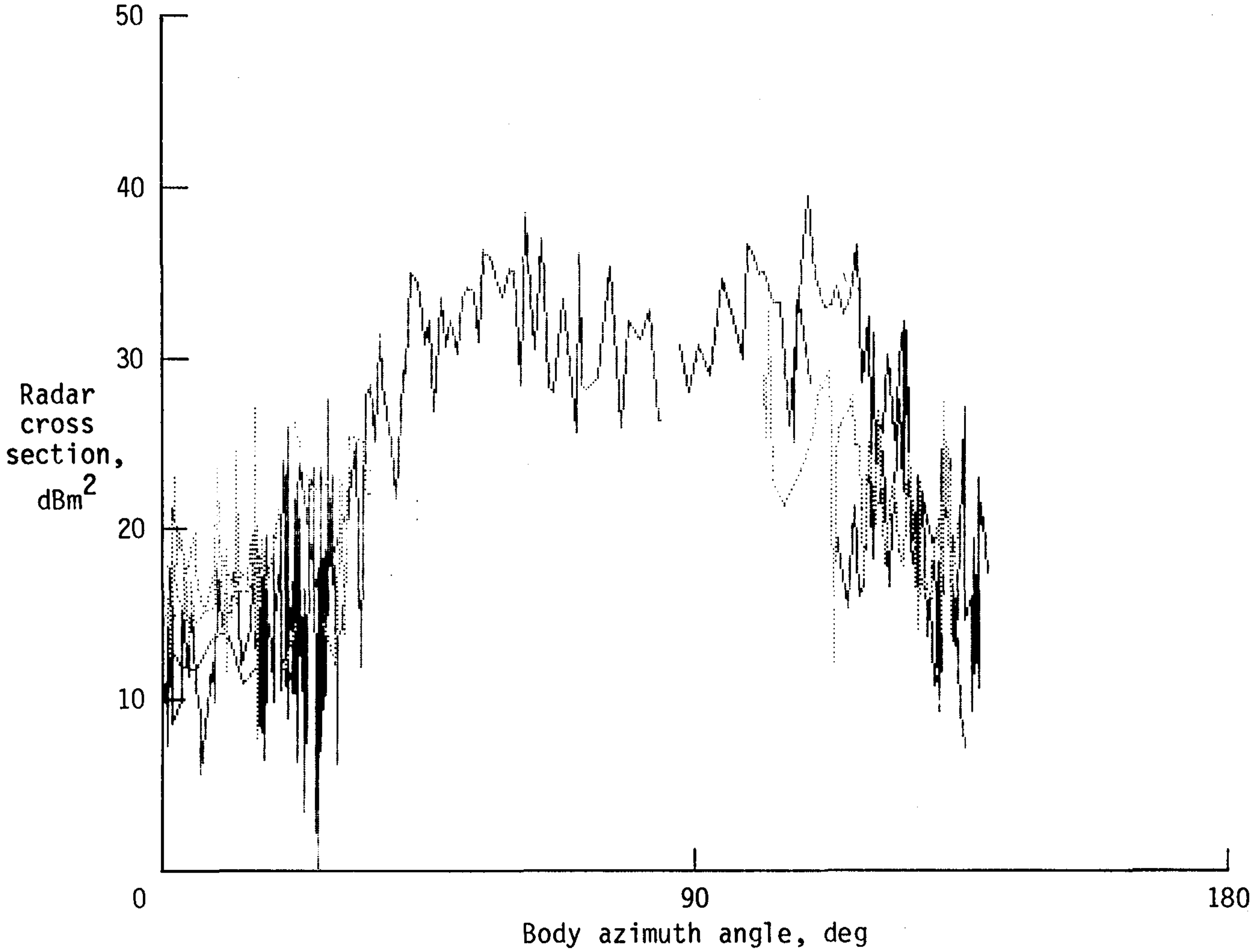

Figure 8. Radar cross section plotted as a function of body azimuth angle for an elevation aspect angle of 0° with an elevation window of ±30°. Based on AN/FPS-16 and AN/MPS-19C radar data; AN/FPS-16 data are shown as dotted line.

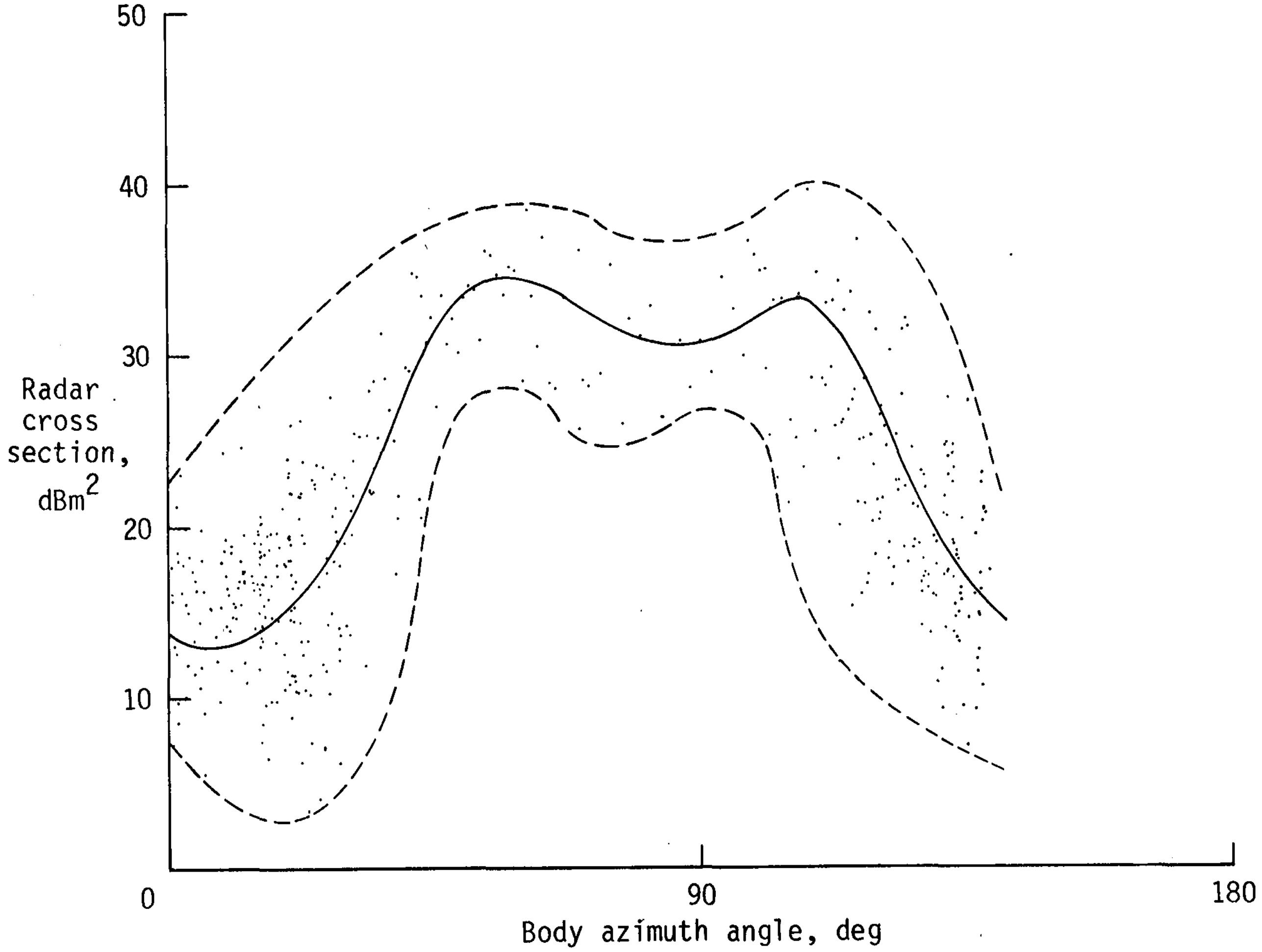

Figure 9. Radar cross section plotted as a function of body azimuth angle for an elevation aspect angle of 0° with an elevation window of ±30°. Based on combined AN/FPS-16 and AN/MPS-19C data.

1. Report No.
NASA TM-72870

2. Government Accession No.

3. Recipient's Catalog No.

4. Title and Subtitle
SHUTTLE ORBITER RADAR CROSS-SECTIONAL ANALYSIS

5. Report Date
October 1979

6. Performing Organization Code

7. Author(s)
Dale W. Cooper and Robert James

8. Performing Organization Report No.
H-1095

9. Performing Organization Name and Address
NASA Dryden Flight Research Center
P. O. Box 273
Edwards, California 93523

10. Work Unit No.

11. Contract or Grant No.
NAS4-2460

12. Sponsoring Agency Name and Address
National Aeronautics and Space Administration
Washington, D.C. 20546

13. Type of Report and Period Covered
Technical Memorandum

14. Sponsoring Agency Code

15. Supplementary Notes

16. Abstract

Measurements of the radar cross section of the space shuttle orbiter were made using AN/MPS-19C and AN/FPS-16 radars during free flight number three of the approach and landing tests at the Dryden Flight Research Center. Excellent cross-section correlation is shown between the two radars. The head-on cross section is found to be approximately 12 to 14 dBm^2 and relatively independent of body elevation angle. Radar cross section may drop slightly, but not significantly, as the aspect angle shifts within 25° of head-on. Broadside cross sections of over 30 dBm^2 were obtained.

17. Key Words (Suggested by Author(s))
Radar
Cross section
Shuttle orbiter
Acquisition

18. Distribution Statement
Unclassified - Unlimited

STAR category: 17

19. Security Classif. (of this report)
Unclassified

20. Security Classif. (of this page)
Unclassified

21. No. of Pages
45

22. Price*
$3.75

For sale by the National Technical Information Service, Springfield, Virginia 22161